Norwegian University
of Life Sciences

Master's Thesis 2023   30 credits
Faculty of Science and Technology

Mass Variations in Antarctica From GRACE and GRACE-FO

Massevariasjoner i Antarktis Fra GRACE og GRACE-FO

Simen Walbækken Tangen
Geomatikk - kart, satellitter og 3D-modellering

NORWEGIAN UNIVERSITY OF LIFE SCIENCES

FACULTY OF SCIENCE AND TECHNOLOGY

DEPARTMENT OF GEOMATICS

Mass Variations in Antarctica From GRACE and GRACE-FO

Author
Simen Walbækken TANGEN

Supervisors:
Christian GERLACH
Vegard OPHAUG

May 15, 2023 (Spring 2023)

Norges miljø- og
biovitenskapelige
universitet

Abstract

Changes on the Earth's surface causes changes in the gravity field. Through dedicated satellite gravity missions such as Gravity Recovery and Climate Experiment (GRACE) and GRACE Follow On (GRACE-FO), this change can be measured. Mass redistribution on the surface of the Earth such as water movement causes these changes. GRACE and GRACE-FO are able to measure several different water cycle mass re-distributions. This thesis will look at the change in the cryosphere in the Antarctic. The cryosphere is highly connected to climate change and is both affected by rising temperatures and affects the global sea level.

The thesis will look at the almost 20-year time series of data from GRACE and GRACE-FO and examine the mass variations. Common errors and corrections will be explained and implemented. The SLR replacement for lower degrees of the GRACE and GRACE-FO solution, GIA modeling and correction, leakage appearance and corrections through a forward modeling method.

There are two main ways to examine GRACE and GRACE-FO data: through spherical harmonic coefficients and through mass concentration blocks. Different approaches to computing a trend from the time series will be looked at and evaluated. The trends will be compared with literature and the different ways of achieving the trend. The mass loss in the Antarctic is computed to be -105 $\pm$ 31 Gt/year from the time period from March 2002 to November 2022. It would appear that trend is decelerating slightly for the last period of time examined.

Sammendrag

Endringer på jordoverflaten forårsaker endringer i gravitasjonsfeltet. Ved hjelp av dedikerte satellitter for å måle gravitasjon, som Gravity Recovery and Climate Experiment (GRACE) og GRACE Follow On (GRACE-FO), kan disse endringene måles. Endringen er en omfordeling av massen på jordoverflaten. GRACE og GRACE-FO kan måle flere forskjellige omfordelinger av masse i den hydrologiske syklusen. Denne oppgaven vil se på endringene i kryosfæren i Antarktis. Denne endringen er sterkt knyttet til klimaendringer og påvirkes både av økende temperaturer og påvirker globalt havnivå.

Oppgaven vil se på nesten 20-års med data fra GRACE og GRACE-FO og undersøke masse-variasjonene. Vanlige feil og korrigeringer vil bli forklart og implementert. SLR-erstatning for lavere grader av GRACE og GRACE-FO-løsningen, GIA-modellering og korrigering, lekkasje og korrigeringer gjennom en "forward modeling" metode.

Det er to hovedmåter å undersøke GRACE og GRACE-FO-data på: gjennom sfæriske harmoniske koeffisienter og gjennom massekonsentrasjonsblokker. Forskjellige tilnærminger til beregning av en trend fra tidsserien vil bli undersøkt og evaluert. Trendene vil bli sammenlignet med litteratur og de ulike måtene trenden er beregnet. Massetapet i Antarktis er beregnet til å være -105 ± 31 Gt/år i tidsperioden fra mars 2002 til november 2022. Det ser ut til at trenden bremser litt ned for den siste perioden som er undersøkt.

Preface

This thesis marks the end of four months of work and of my 5 years as a student at the Norwegian University of Life Sciences (NMBU).

The polar areas have always been of great interest to me, so it is with great gratitude that I was given the opportunity to write this thesis. I want to sincerely thank my supervisors Christian Gerlach and Vegard Ophaug. They have given me insight and guidance which have abled me to write this thesis. I am truly grateful for all the help and feedback during the last year.

I am happy for all the experiences I have had in my time at NMBU both academically and socially. From an academic perspective, I would highlight partaking in publishing a peer-review paper with Ola Øvstedal and co-presenting it at the XXVII FIG Congress 2022 in Warsaw. From the social perspective, it has been great to get to know a variety of people and learn new skills, outside the fields of my study.

My fellow master students in "mastersalen" need to be thanked for inspiration and good camaraderie during the last 4 months.

I want to thank friends, family, and my dearest Guro for their support and motivation through this thesis, and lastly thanks to the dog Dina for long refreshing walks to clear my head.

Simen Walbækken Tangen
Ås, 15.05.2023

Contents

List of Figures

List of Tables

Chapter 1

Introduction

1.1 Motivation

Understanding the changes in climate is crucial to understand the implications it creates for life on Earth. UN's sustainability goal number 13 i s to *Take urgent action to combat climate change and its impacts*. To be able to fulfill this goal it is important to properly measure and understand the trend and variations in the variables that contribute to climate change. The melting of polar ice sheets is a substantial contributor to rising sea-level and changes in the water cycle. This thesis will look at the ice sheets in Antarctica.

Antarctica is the most hazardous continent on Earth with an extreme environment and a remote location. The early explorations to Antarctica were challenging and often deadly, and still present a formidable obstacle for scientific research today. Mapping Antarctica terrestrially is a demanding task, however, with the use of space surveying methods, the whole continent is possible to measure with less effort and with great detail. The Gravity Recovery And Climate Experiment(GRACE) and GRACE Follow-On(GRACE-FO) gravity missions have provided almost two decades of global mass variations data, therefore it's suitable to find the mass variations and trends in Antarctica

The applications from GRACE and GRACE-FO are varied. They survey the mass variations, and the water mass variations can be connected to the climate system. These segments below are partially based on Chen et al. (2022) and Tapley et al. (2019).

GRACE and GRACE-FO can measure terrestrial water storage (TWS) change without separating the different compartments, which are surface waters, the upper few meters of soil, and groundwater. The global scale measurements can be compared to global hydrological models made without the GRACE and GRACE-FO data. The TWS changes at different river basins can also be compared to in-situ measurements. TWS change has variations that are complex and at interannual and decadal timescales. This makes it harder to discover trends from climate change and other geophysical signals. The recent droughts in Europe, Southeast Brazil, and Southwestern U.S. can be seen in TWS trends from GRACE and GRACE-FO. Furthermore shifts from dry to wetter conditions can be detected around the globe.

Mass variations of polar ice sheets and glaciers can be measured with GRACE and GRACE-FO. Many studies have looked at mass variations at the Greenland Ice Sheet (GrIS) and the

Antarctic Ice Sheet (AIS). Since the resolution of the GRACE and GRACE-FO models are low, some studies combine altimetry, space-borne interferometric synthetic aperture radar (InSAR), and satellite gravimetry. In this study only GRACE and GRACE-FO data will be used.

The Global Mean Oceanic Mass Change can also be measured from GRACE and GRACE-FO. It's possible to directly estimate the barystatic sea level on a monthly basis with GRACE and GRACE-FO.

Apart from the water mass variations, GRACE and GRACE-FO are also able to measure mass variations as a result of GIA, seismic activities, earthquakes, and possible deep-earth signals. The GIA measured must be subtracted for TWS and mass variations for the polar regions to get accurate estimates.

1.2 Objective

The ambition of this thesis is to find the mass variations and trends in the cryosphere in Antarctica with the use of data collected by the GRACE and GRACE-FO gravity missions.

The principle of measurement with the GRACE and GRACE-FO and their components will be explained. This thesis will delve into the challenges and errors which emerge using GRACE and GRACE-FO data and the possible solutions. Different processing centers offer various solutions to the user community for the GRACE time series, which can be accessed as mass concentration blocks or a series of spherical harmonic coefficients.

This thesis closely follows the work by Loomis et al. (2021) where the closeness of the present results to their study is taken as a proof of concept. The same data and processing steps as in Loomis et al. (2021) will be used to compute a mass trend for Antarctica for the 2002-2016 time period (using GRACE data only). Once the goal of proof-of-concept is investigated, a second goal is to extend this time series to 2022 using GRACE-FO data. A third goal will be to investigate if the mass trends in Antarctica are accelerating, stable, or decelerating.

The Antarctic Ice Sheet(AIS) is commonly divided into three areas: West Antarctic Ice Sheet(WAIS), East Antarctic Ice Sheet(EAIS), and The Antarctic Peninsula(AP). The areas can be seen in Figure 1.1, in this thesis the areas defined in Rignot et al. (2011) are used and are the same areas used in Loomis et al. (2021).
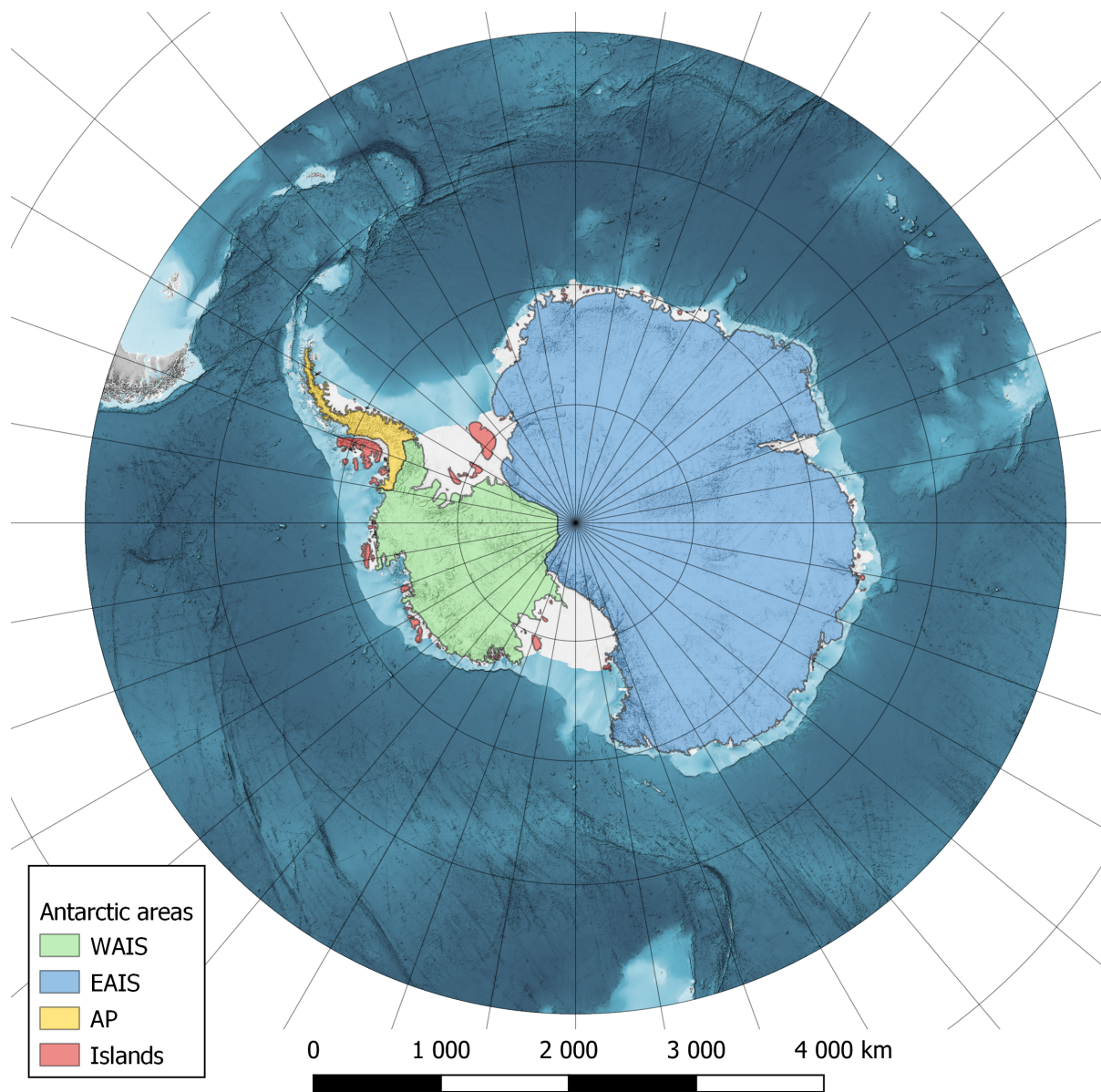
Figure 1.1: Areas that are chosen in this thesis. WAIS is the West Antarctic Ice Sheet, EAIS is the East Antarctic Ice Sheet, AP is the Antarctic Peninsula and Islands are the islands on the coast of the Antarctic continent. The Islands are not used for mass estimates in this thesis. Areas from Rignot et al. (2011), background map from Dorschel et al. (2022)

1.3 Thesis summary

This thesis consists of 6 chapters and a short summary of them is presented here:

- **Chapter 1: Introduction:** This chapter introduces the motivation and objective of the thesis.

- **Chapter 2: The gravity field of the Earth:** This chapter establishes the theory that is the basis for the computation in this thesis. The different parts of the gravity signal is also explained.

- **Chapter 3: Technology and Computational Methods:** This chapter introduces the satellite gravity missions, filtering techniques, lower degrees replacement, trend calculation, and leakage correction using a forward modeling schema.

- **Chapter 4: Results:** In this chapter presents: (i) A proof of concept including only GRACE data. (ii) Include GRACE-FO data that is not a part of the proof of concept.

- **Chapter 5: Discussion:** This chapter discusses the results, both the expected and the unexpected. Possible courses for the unexpected are described.

- **Chapter 6: Conclusions:** This chapter includes conclusions and recommendations for further work.

1.4 Abbreviations

Abbreviation	Explanation
GRACE	Gravity Recovery and Climate Experiment
GFO	GRACE Follow-On, GRACE-FO
GIA	Glacial Isostatic adjustment
PGR	Post Glacial Rebound
EOP	Earth Orientation Parameters
LEO	Low Earth Orbit
MEO	Mean Earth Orbit
SST-HL	Satellite-to-Satelite Tracking in High-Low mode
SST-LL	Satellite-to-Satelite Tracking in Low-Low mode
SGG	Satellite Gravity Gradiometry
EWH	Equivalent Water Height
GrIS	Greenland Ice Sheet
AIS	Antarctic Ice Sheet
WAIS	West Antarctic Ice Sheet
EAIS	East Antarctic Ice Sheet
AP	Antarctic Peninsula
GNSS	Global Navigation Satellite Systems
ACC	Superstar Accelerometer
KBR	K-Band Ranging
TWS	Terrestrial Water Storage
SDS	The GRACE/GRACE-FO Science Data System: CSR, GFZ and JPL
CSR	Center for Space Research at the University of Texas at Austin
GFZ	German Research Centre for Geosciences
JPL	NASA's Jet Propulsion Laboratory
ICGEM	International Centre for Global Earth Models
COST-G	Combination Service for Time-variable Gravity Fields
GSM	Monthly GRACE/GRACE-FO Gravity Solution
AOD	Atmospheric and Oceanic De-aliasing
RDC	Raw Data Center
DLR	Deutsches zentrum für Luft und Raumfahrt (German Aerospace Center)
GSFC	Goddard Space Flight Center -NASA
MASCON	Mass Concentration blocks
DDK	Denoising and Decorrelation Kernel
SHA	Spherical Harmonic Analysis
SHS	Spherical Harmonic Synthesis
FM	Forward modeling

Chapter 2

The gravity field of the Earth

2.1 Important definitions

Physical geodesy has a basis in Newton's law of attraction (2.1). Two masses M(Earth) and m which are separated by the distance r are attracted to each other with the mutual force $\vec{F}$

$$\vec{F} = -G\frac{M \cdot m}{r^2}\hat{r} \tag{2.1}$$

G is the universal gravitational constant($G = 6.6742 \cdot 10^{-11} \mathrm{m^3 kg^{-1} s^{-2}}$) and $\hat{r}$ is the unit vector and given as $\hat{r} = \vec{r}/r$.
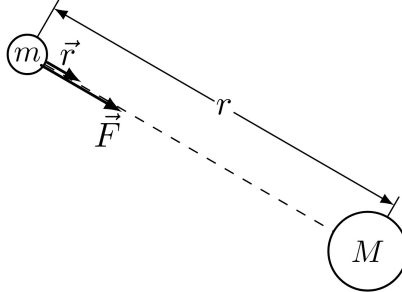
Figure 2.1: A 2-dimensional visualisation of the attraction between from the mass M and effecting the mass m

With Newton's second law: $\vec{F} = m\vec{g}$, the force $\vec{F}$ can be replaced by the gravitational acceleration $\vec{g}$ felt by the mass m. This transforms Newton's law of attraction (2.1) into equation (2.2).

$$\vec{g} = -\frac{GM}{r^2}\hat{r} \tag{2.2}$$

The gravitational field is conservative. The potential energy is unchanged for a body of mass that is moved from point P to another point and back to point P. This means that potential energy in the gravitational field is path independent, and $\vec{g}$ can be described as a gradient vector of the scalar potential function V, see Hofmann-Wellenhof and Moritz (2006).

$$\vec{g} = \nabla V = \frac{\partial V}{\partial x}\hat{i} + \frac{\partial V}{\partial y}\hat{j} + \frac{\partial V}{\partial z}\hat{k} \tag{2.3}$$

Equation (2.3) is given in cartesian coordinates and has $\hat{i}$, $\hat{j}$ and $\hat{k}$ which are unit vectors in the direction of x, y and z. It is easier to use the gravitational potential V instead of the acceleration $\vec{g}$. This is given in equation (2.4) and implies that the attracting masses is superposition the effect of multiple sources of multiple point masses $m_1, m_2, ..., m_i$, which are inside the Earth's surface. Hofmann-Wellenhof and Moritz (2006)

$$V = G \sum_{i=1}^{n} \frac{m_i}{r} \tag{2.4}$$

When assuming that the point masses are continuously distributed inside the Earth's surface, integration through the Earth could be applied and transforms equation (2.4) into Newton's integral (2.5).

$$V = G \iiint_v \frac{dm}{r} = G \iiint_v \frac{\rho}{r} \, dv \tag{2.5}$$

In Newton's integral (2.5), $\rho = \frac{dm}{dv}$ is implemented to obtain the right side. ρ is the density, dm are an element of mass, and dv is an element of volume. The problem with Newton's integral is that the Earth's density(ρ) is not exactly known. The potential is better described as a differential equation which is better suited when working with boundary value problems.

Inside the Earth, the density will change discontinuously, and the potential satisfies Poisson's equation:

$$\Delta V = \frac{\partial^2 V}{\partial x^2} + \frac{\partial^2 V}{\partial y^2} + \frac{\partial^2 V}{\partial z^2} = -4\pi G \rho \tag{2.6}$$

Δ stands for the Laplacian operator $\frac{\partial^2}{\partial x^2} + \frac{\partial^2}{\partial y^2} + \frac{\partial^2}{\partial z^2}$. For points outside the Earth's surface, the density ρ becomes zero, and Poisson's equation is reduced to the Laplace differential equation:

$$\Delta V = \frac{\partial^2 V}{\partial x^2} + \frac{\partial^2 V}{\partial y^2} + \frac{\partial^2 V}{\partial z^2} = 0 \tag{2.7}$$

The Laplace equation's solutions are harmonic solutions. This means the gravitational field outside the Earth's surface is given as a harmonic function.

2.2 Spherical harmonic representations

The density of the Earth is not exactly known, and the gravitational potential V can not be computed with Newton's integral (2.5). Nevertheless, it is possible to get a convergent series expansion of V in the exterior space of the Earth as a special solution of (2.7). We start with the reciprocal distance function between computation point P and source point Q, $1/l_{PQ} = 1/\sqrt{(r_P^2 + r_Q^2 - 2r_P r_Q \cos \psi_{PQ})}$, and its an expansion into Legendre polynomials:

$$\frac{1}{l_{PQ}} = \frac{1}{r_P} \sum_{n=0}^{\infty} \left(\frac{r_Q}{r_P}\right)^n P_n(\cos \psi) \tag{2.8}$$

8

where $P_n(\cos \psi)$ is the unnormalized Legendre polynomial and $r_p > r_Q$. The spherical harmonic addition theorem gives the relationship between the Legendre polynomial and the surface spherical harmonics:

$$P_n(\cos \psi) = \frac{1}{2n+1} \sum_{m=0}^{n} [\bar{\mathcal{R}}_{nm}(\theta_P, \lambda_P)\bar{\mathcal{R}}_{nm}(\theta_Q, \lambda_Q) + \bar{\mathcal{S}}_{nm}(\theta_P, \lambda_P)\bar{\mathcal{S}}_{nm}(\theta_Q, \lambda_Q)] \tag{2.9}$$

where $\bar{\mathcal{R}}_{nm}(\theta, \lambda) = \bar{P}_{nm}(\cos \theta) \cos m\lambda$ and $\bar{\mathcal{S}}_{nm}(\theta, \lambda) = \bar{P}_{nm}(\cos \theta) \sin m\lambda$ are the normalized surface harmonic functions.

Equation (2.9) can be inserted into equation (2.8) and equation (2.10) is obtained.

$$\frac{1}{l_{PQ}} = \frac{1}{r_P} \sum_{n=0}^{\infty} \left(\frac{r_Q}{r_P}\right)^n \frac{1}{2n+1} [\bar{\mathcal{R}}_{nm}(\theta_P, \lambda_P)\bar{\mathcal{R}}_{nm}(\theta_Q, \lambda_Q) + \bar{\mathcal{S}}_{nm}(\theta_P, \lambda_P)\bar{\mathcal{S}}_{nm}(\theta_Q, \lambda_Q)] \tag{2.10}$$

If then Newton's integral (2.5) express the potential from several source point Q to the computation point P.

$$V(P) = G \iiint_v \frac{\rho(Q)}{l_{PQ}} \, dv \tag{2.11}$$

Equation (2.10) can be inserted into the Newtons integral (2.11) which gives

$$V(P) = G \iiint_v \rho(Q) \left[\frac{1}{r_P} \sum_{n=0}^{\infty} \left(\frac{r_Q}{r_P}\right)^n \frac{1}{2n+1} \sum_{m=0}^{n} (\bar{\mathcal{R}}_{nm}(\theta_P, \lambda_P)\bar{\mathcal{R}}_{nm}(\theta_Q, \lambda_Q) + \right.$$
$$\left. \bar{\mathcal{S}}_{nm}(\theta_P\lambda_P)\bar{\mathcal{S}}_{nm}(\theta_Q, \lambda_Q)) \right] dv \tag{2.12}$$

Further, by changing integration and summation and separating the terms depending on P and Q, the equation (2.12) can be given as

$$V(P) = G \sum_n \sum_m \frac{1}{r_P^{n+1}} \left[\bar{\mathcal{R}}_{nm}(\theta_P, \lambda_P) \frac{1}{2n+1} \iiint_v r_Q^n \bar{\mathcal{R}}_{nm}(\theta_Q, \lambda_Q)\rho(Q)dv + \right.$$
$$\left. \bar{\mathcal{S}}_{nm}(\theta_P, \lambda_P) \frac{1}{2n+1} \iiint_v r_Q^n \bar{\mathcal{S}}_{nm}(\theta_Q, \lambda_Q)\rho(Q)dv \right] \tag{2.13}$$

By dividing equation 2.13 with $M \cdot R^n$, the Q-dependent terms will give the dimensionless, normalized spherical harmonic coefficients:

$$\left\{ \begin{matrix} \bar{C}_{nm} \\ \bar{S}_{nm} \end{matrix} \right\} = \frac{1}{M(2n+1)} \iiint_v \left(\frac{r_Q}{R}\right)^n \rho(Q) \left\{ \begin{matrix} \bar{\mathcal{R}}_{nm}(\theta_Q, \lambda_Q) \\ \bar{\mathcal{S}}_{nm}(\theta_Q, \lambda_Q) \end{matrix} \right\} dv \tag{2.14}$$

Thus the spherical harmonic coefficients $\bar{C}_{nm}$ and $\bar{S}_{nm}$ are determined by global integration the density function $\rho(Q)$ multiplied with the surface spherical harmonic functions $\bar{\mathcal{R}}_{nm}$ and $\bar{\mathcal{S}}_{nm}$.

We obtain a series expansion of Earth's gravitational potential by considering equation (2.14) and equation (2.13) multiplied with $M \cdot R^n$;

$$V_P(r, \theta, \lambda) = \frac{GM}{R} \sum_{n=0}^{\infty} \left(\frac{R}{r}\right)^{n+1} \sum_{m=0}^{n} (\bar{C}_{nm} \cos m\lambda + \bar{S}_{nm} \sin m\lambda) \bar{P}_{nm}(\cos \theta) \qquad (2.15)$$

R is the mean Earth radius. An upward continuation is made possible through $\left(\frac{R}{r}\right)^{n+1}$ and allows us to compute the potential at points situated above the Earth's surface. r is the geocentric radius of the computation point P. $\bar{C}_{nm}$ and $\bar{S}_{nm}$ are dimensionless potential coefficients. $\bar{P}_{nm}(\cos \theta)$ is the Legendre function, which is used to describe signals on a sphere. The degree and order are subsequently n and m. Harmonics of low degree and order numbers represent long spatial wavelengths and describe the large-scale features of the signal. Harmonics of high degree and order represent short wavelengths and describe smaller details. The coeffisents $\bar{C}_{nm}$ and $\bar{S}_{nm}$ allows to reconstruct a global signal.

The way of calculating the potential described in equation 2.15 is described as the spherical harmonic synthesis (SHS). The way of obtaining spherical harmonic coefficients $\bar{C}_{nm}$ and $\bar{S}_{nm}$ as described in equation 2.14 is the spherical harmonic analysis (SHA) and can be described as the inverse operation to SHS.

Determining the gravitational potential through equation 2.15 and determining the masses and density is known as the *inverse problem of potential theory*. This inverse problem has an ambiguity which implies that it doesn't have any unique solutions, since there are endless possible mass distributions which can give the same gravitational potential P. Therefore additional data from geological and geophysical is required to interpret the gravity field properly.

2.2.1 Disturbing potential and quantities of the gravity field

The force acting on a body on the surface of the Earth is the superposition of the gravitational force and the centrifugal force caused by Earth's rotation

Therefore we need to operate with gravity potential W, which consists of the gravitational potential V and centrifugal potential Z as seen in equation (2.16).

$$W = V + Z \qquad (2.16)$$

V can be given in the Newtons integral (2.5). Z depends on the distance from the Earth's rotation axis to the computation point and can be given by its location x, y and the Earth's angular velocity ω. This gives equation (2.17).

$$W = G \iiint_v \frac{\rho}{r}, dv + \frac{1}{2}\omega^2(r \sin \theta)^2 \qquad (2.17)$$

To approximate the geometry of the real earth there are two important concepts, the geoid and the ellipsoid. The geoid was defined by Gauss in 1828 as the "equipotential surface of the Earth's gravity field coinciding with the mean sea level of the oceans" (Torge and Müller, 2012). The geoid is ever-changing because of the geophysical processes affecting the gravitational field. The ellipsoid is a geometric shape that resembles the earth. The height difference between these is referred to as the geoid height.

A normal potential U can be derived using an ellipsoid as a geodetic reference system and a model for the Earth's masses

$$U = V^N + Z \qquad (2.18)$$

where V^N is the normal gravitational potential deriving from the ellipsoid. The disturbing potential can then be calculated by taking the difference between the gravity and normal potential (2.19). The centrifugal acceleration Z is known with high accuracy. When calculating the disturbing potential, the centrifugal part of gravitational and normal potential are assumed to have equal values.

$$T = W - U = (V + Z) - (V^N + Z) = V - V^N \qquad (2.19)$$

The gravitational and normal potential are harmonic outside the Earth; therefore, the disturbing potential will also be harmonic outside the Earth. Then it obeys the Laplace equation (2.7) and gives:

$$\Delta T = 0 \qquad (2.20)$$

The disturbing potential can be expanded into a spherical harmonic function equation (2.21).

$$T(r, \theta, \lambda) = \frac{GM}{R} \sum_{n=2}^{\infty} \left(\frac{R}{r}\right)^{n+1} \sum_{m=0}^{n} (\Delta \bar{C}_{nm} \cos m\lambda + \Delta \bar{S}_{nm} \sin m\lambda) \bar{P}_{nm}(\cos \theta) \qquad (2.21)$$

The summation starts at $n = 2$, assuming that the Earth and the ellipsoid have equal masses and that their centres of mass coincide. The $\Delta \bar{C}_{nm}$ and $\Delta \bar{S}_{nm}$ are the differences in potential coefficients of the real and normal gravitational field. Since the normal potential field only varies with the latitude and is symmetric around the equator, it contains only even degree coefficients of order $n = 0$. Therefore it holds

$$\Delta \bar{C}_{nm} = \begin{cases} \bar{C}_{nm} - \bar{C}_{nm}^N & \text{if } m = 0 \text{ and } n \in 2, 4, 6, \ldots, n_{\max} \\ \bar{C}_{nm} & \text{else} \end{cases} \qquad (2.22)$$
$$\Delta \bar{S}_{nm} = \bar{S}_{nm}$$

Where $n_{\max}$ is the maximal degree of the solution (Hofmann-Wellenhof and Moritz, 2006).

The spherical harmonic representation of disturbing potential (2.21) can be derived into several other quantities as; geoid height (N), gravity anomalies (Δg), or first (T_r) and second-order (T_{rr}) radial derivatives, as seen in Table 2.1

Table 2.1: Spherical harmonic functions of different quantities of the gravity field

T	$=$	$\frac{GM}{R}$	$\sum_{n=2}^{\infty}$	$\left(\frac{R}{r}\right)^{n+1}$		$\sum_{m=0}^{n}(\Delta \bar{C}_{nm} \cos m\lambda + \Delta \bar{S}_{nm} \sin m\lambda) \bar{P}_{nm}(\cos \theta)$
N	$=$	R	$\sum_{n=2}^{\infty}$			$\sum_{m=0}^{n}(\Delta \bar{C}_{nm} \cos m\lambda + \Delta \bar{S}_{nm} \sin m\lambda) \bar{P}_{nm}(\cos \theta)$
Δg	$=$	$\frac{GM}{R^2}$	$\sum_{n=2}^{\infty}$	$\left(\frac{R}{r}\right)^{n+2}$	$(n-1)$	$\sum_{m=0}^{n}(\Delta \bar{C}_{nm} \cos m\lambda + \Delta \bar{S}_{nm} \sin m\lambda) \bar{P}_{nm}(\cos \theta)$
T_r	$=$	$\frac{GM}{R^2}$	$\sum_{n=2}^{\infty}$	$\left(\frac{R}{r}\right)^{n+2}$	$(n+1)$	$\sum_{m=0}^{n}(\Delta \bar{C}_{nm} \cos m\lambda + \Delta \bar{S}_{nm} \sin m\lambda) \bar{P}_{nm}(\cos \theta)$
T_{rr}	$=$	$\frac{GM}{R^3}$	$\sum_{n=2}^{\infty}$	$\left(\frac{R}{r}\right)^{n+3}$	$(n+1)(n+2)$	$\sum_{m=0}^{n}(\Delta \bar{C}_{nm} \cos m\lambda + \Delta \bar{S}_{nm} \sin m\lambda) \bar{P}_{nm}(\cos \theta)$

2.2.2 Changing surface mass and equivalent water height

The surface the Earth and its variations are the aspects of the gravity signal that is the main interest of this study. To get there, we need to use the equation for geoid height given in table (2.1), describe the geoid shape N:

$$N = R \sum_{n=2}^{\infty} \sum_{m=0}^{n} (\bar{C}_{nm} \cos m\lambda + \bar{S}_{nm} \sin m\lambda) \bar{P}_{nm}(\cos \theta) \tag{2.23}$$

The time-dependent change in the geoid shape can be expressed as:

$$\delta N = R \sum_{n=2}^{\infty} \sum_{m=0}^{n} (\delta \bar{C}_{nm} \cos m\lambda + \delta \bar{S}_{nm} \sin m\lambda) \bar{P}_{nm}(\cos \theta) \tag{2.24}$$

It's important to differentiate between the $\delta \bar{C}_{nm}$ and $\delta \bar{S}_{nm}$ in this section where it describes the change over time and $\Delta \bar{C}_{nm}$ and $\Delta \bar{S}_{nm}$ in the section above where it describes the change between the real and normal gravitational field.

This geoid change is caused by variations in the solid earth and a thin layer on the surface of the Earth, which includes the ice caps, oceans, terrestrial water storage, and the atmosphere. The change in the thin layer loads on the solid earth and deforms it and makes a deformation potential. Therefore we can split the changing geoid signal into two components:

$$\begin{Bmatrix} \delta \bar{C}_{nm} \\ \delta \bar{S}_{nm} \end{Bmatrix} = \begin{Bmatrix} \delta \bar{C}_{nm} \\ \delta \bar{S}_{nm} \end{Bmatrix}_{surfmass} + \begin{Bmatrix} \delta \bar{C}_{nm} \\ \delta \bar{S}_{nm} \end{Bmatrix}_{solidE} \tag{2.25}$$

The change in surface mass can be conceived as a change in the density $\delta \rho(r, \theta, \lambda)$ within the thin layer that defines the surface mass. The change in surface density $\delta \sigma$ can be defined as a radial integral of $\delta \rho$ through the thin layer.

$$\delta \sigma(\theta, \lambda) = \int_{thinlayer} \Delta(r, \theta, \lambda) dr \tag{2.26}$$

The following section follows the equations given in Wahr and Molenaar (1998). By summation over (n, m) in equation (2.24) it can be truncated to $n < n_{max}$. If the thin layer has a thickness H and is thin enough that $(n_{max} + 2)H/R << 1$. Then $(r/R)^{l+2} \approx 1$, and the coefficients for surface mass are given by equation (2.27).

$$\begin{Bmatrix} \delta \bar{C}_{nm} \\ \delta \bar{S}_{nm} \end{Bmatrix}_{surfmass} = \frac{3}{4\pi R \rho_{ave}(2n+1)} \int_V \delta \sigma(\theta, \lambda) \times \bar{P}_{nm}(\cos(\theta)) \begin{Bmatrix} \delta \cos(m\lambda) \\ \delta \sin(m\lambda) \end{Bmatrix} \sin \theta d\theta d\lambda \tag{2.27}$$

Where ρ_{ave} is the average density of the Earth. Equation (2.27) describes the direct gravitational attraction from the surface mass that will affect the geoid. Another geoid contribution is from the deforming and loading on the solid Earth caused by the surface mass. This has a linear connection to Equation (2.27) and can be implemented by multiplying with k_n.

$$\begin{Bmatrix} \delta \bar{C}_{nm} \\ \delta \bar{S}_{nm} \end{Bmatrix}_{solidE} = \frac{3k_n}{4\pi R \rho_{ave}(2n+1)} \int_V \delta \sigma(\theta, \lambda) \times \bar{P}_{nm}(\cos(\theta)) \begin{Bmatrix} \delta \cos(m\lambda) \\ \delta \sin(m\lambda) \end{Bmatrix} \sin \theta d\theta d\lambda \tag{2.28}$$

k_n is the load Love numbers of the degree n, the loading effect will be explained in more detail in section 2.3.1. From the realisation in equation (2.27) and (2.28), equation (2.29) is obtainable.

$$\delta\sigma(\theta,\lambda) = \frac{R\rho_{ave}}{3} \sum_{n=2}^{N} \sum_{m=0}^{n} \frac{2n+1}{1+k_n} \bar{P}_{nm}(\cos\theta) \left[\delta\bar{C}_{nm}\cos m\lambda + \delta\bar{S}_{nm}\sin m\lambda \right] \qquad (2.29)$$

The change in surface mass $\delta\sigma$ is given in kg/m^2, as seen in equation (2.29) the summation is $\sum_{n=2}^{N}$ where N represent the maximum spherical harmonic degree, also referred to as N_{max}. If the solution of equation (2.29) is divided by the density of water ρ_w assumed to be 1000 kg/m^3, then $\delta\sigma/\rho_w$ equals the equivalent water height(EWH) in meter.

Equation (2.29) contains the Earth density ρ_{ave}, which can be replaced by $\rho_{ave} = \frac{M_E}{V_E}$. Considering $V_E = \frac{4}{3}\pi R^3$, equation (2.29) can be rewritten in the following form equation (2.30) as given by Chen et al. (2015).

$$\delta\sigma(\theta,\lambda) = \frac{M_E}{4\pi R^2} \sum_{n=2}^{N} \sum_{m=0}^{n} \frac{2n+1}{1+k_n} \bar{P}_{nm}(\cos\theta) \left[\delta\bar{C}_{nm}\cos m\lambda + \delta\bar{S}_{nm}\sin m\lambda \right] \qquad (2.30)$$

As mentioned before, the inverse problem is where we don't know the density entirely and can describe equation (2.30). Despite that, if we know or have estimates of the change in density, the equations (2.27) and (2.28) we can do an SHA to obtain the spherical harmonic coefficient and we get equation (2.31) as given in Chen et al. (2015) and quite similar to equation (2.14) however equation (2.31) is on the surface, so $(r/R)^2 = 1$ and can be left out.

$$\begin{Bmatrix} \delta\bar{C}_{nm} \\ \delta\bar{S}_{nm} \end{Bmatrix} = \frac{R^2}{M_E} \frac{k_n+1}{2n+1} \sum_{i=1}^{180/\Delta\lambda} \sum_{j=1}^{360/\Delta\theta} \Delta\sigma(\theta_i,\lambda_j)\bar{P}_{nm}(\cos\theta) \begin{Bmatrix} \cos m\lambda_j \\ \sin m\lambda_j \end{Bmatrix} \sin\theta_i\Delta\theta\Delta\lambda \quad (2.31)$$

Equation (2.31) the $\Delta\sigma$ is summed up around the Earth with the spherical coordinates (θ,λ). The $\Delta\theta$ and $\Delta\lambda$ are the spatial resolutions of the spherical coordinates.

2.2.3 Statistics related to spherical harmonic synthesis

To compute the uncertainties in this thesis the equations for error propagation are obtained from Gerlach and Fecher (2012). The propagating error variances between computation point P and source point Q can be computed with

$$Cov(N_P, N_Q) \approx R^2 \sum_{m=0}^{N} \left[\left(\sum_{n=m}^{N} Var(\bar{C}_{nm})\bar{P}_{nm}(\cos\theta_P)\bar{P}_{nm}(\cos\theta_Q) \right) \cos m\lambda_P \cos m\lambda_Q + \left(\sum_{l=m}^{N} Var(\bar{S}_{nm})\bar{P}_{nm}(\cos\theta_P)\bar{P}_{nm}(\cos\theta_Q) \right) \sin m\lambda_P \sin m\lambda_Q \right] \qquad (2.32)$$

This thesis will look at the variance at computation point P so be replacing Q by P, thereby squaring some of the factors

$$Var(N_P) \approx R^2 \sum_{m=0}^{N} \left[\left(\sum_{l=m}^{N} Var(\bar{C}_{nm})(\bar{P}_{nm}(\cos\theta_P))^2 \right) (\cos m\lambda_P)^2 + \right.$$
$$\left. \left(\sum_{n=m}^{N} Var(\bar{S}_{nm})(\bar{P}_{nm}(\cos\theta_P))^2 \right) (\sin m\lambda_P)^2 \right]$$

(2.33)

By implicating equation (2.33) we can now compute the variance on a given point on the sphere. This can be used in combination with equation (2.30) to compute the formal standard deviation in EWH.

2.3 Gravity variations and geophysical signals

There is a range of both geophysical and astronomical processes that affect the surface geometry, orientation, and gravity field of the Earth. The timescale of these processes and their effects vary from minutes and hours (co-seismic deformation) to decades (sea-level change) and secular events (GIA, ice cover changes, tectonic plate movements). How they affect the Earth's system and are measured also varies; see figure(2.2).
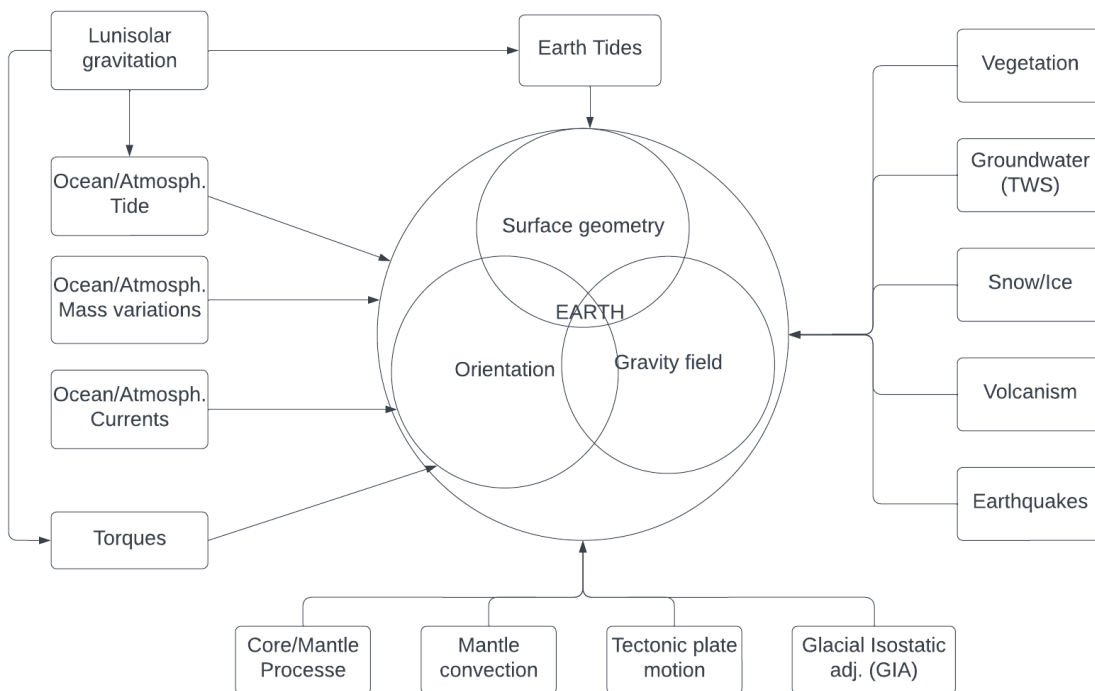
Figure 2.2: Geophysical and astronomical processes and their effect on the Earth's surface geometry, gravity field and orientation. Inspired by Fig. 8.14 in Torge and Müller (2012)

This section will look into the effects that are relevant to the topic of this thesis.

2.3.1 Loading and tidal effects

The loading effect results from masses that move around on the Earth's surface, primarily ocean and atmosphere masses. They have a gravitational pull that affects gravitational measurements, and the masses deform the Earth's surface geometry. There are tidal loading effects and non-tidal loading effects. Tidal effects occur because of the gravitational pull of the Moon and the Sun. It affects the oceans, the atmosphere, and even the solid Earth itself, which behaves like an elastic body. The tidal forces can be split into two parts; the time-varying, where the mean value over time is zero and a permanent tidal where the mean value over time is not zero because of the existence of the Moon and Sun.

There are three definitions when the tidal forces are brought into geoid calculations.

- Mean tide is when the time-varying tide forces are removed with models or with the mean of a long time series. It includes the effect of the masses' gravitational pull and the deformation.

- Zero tide, where also the gravitational pull from the permanent tide is eliminated, but the permanent deformation is retained.

- Tide free is where also the permanent deformation is removed, and therefore the total tidal effect is eliminated. Determining the deformation involves geophysical modeling, which requires load love numbers.

Zero tides are preferred in geodesy. This is because the gravitational pull of the Moon and the Sun don't coincide with the boundary value problems where the only attracting mass is the Earth. (Torge and Müller, 2012).

As mentioned in Changing surface mass and equivalent water height section (2.2.2), the load love numbers will be explained in more detail here. The load love numbers are dimensionless coefficients depending on the degree n and describe the deformation and potential change of the elastic Earth. Its obtained through computation of the tidal potential. In this study, the love numbers are from Table 1. in Wahr and Molenaar (1998)

2.3.2 GIA

This section is based on the presentation of Torge and Müller (2012) and Whitehouse (2018). Glacial Isostatic Adjustment (GIA) refers to the response of the solid Earth's surface, the gravitational field, and the oceans to the expansion and reduction of ice sheets.

During a glacial cycle, the weight of water masses as ice and liquid water deforms and subdues the lithosphere. The lithosphere is the Earth's crust and the upper part of the mantle and is between 70-150 km thick, depending on the location. It is viscous, making it deform when masses increase above and allowing it to rebound when the masses are removed. It is called an isostatic deformation when the crust maintains an equilibrium between the lithosphere and mantle. The glacial cycle has a periodicity of 100 000 years, the growth of an ice sheet and its volume happens gradually over tens of thousands of years, but the retreat happens over just a few thousand years.

The last ice age ended 12 000- 20 000 years ago, and when the ice masses retreated the lithosphere got in an imbalance and was pushed upwards by the mantle. This made the areas affected experience a land uplift and experience sea-level change. The effects were initially rapid and gradually decreased over time but are still observable today. The effects after ice sheets retreat are called a post-glacial rebound(PGR). These effects can be seen in Figure 2.3.
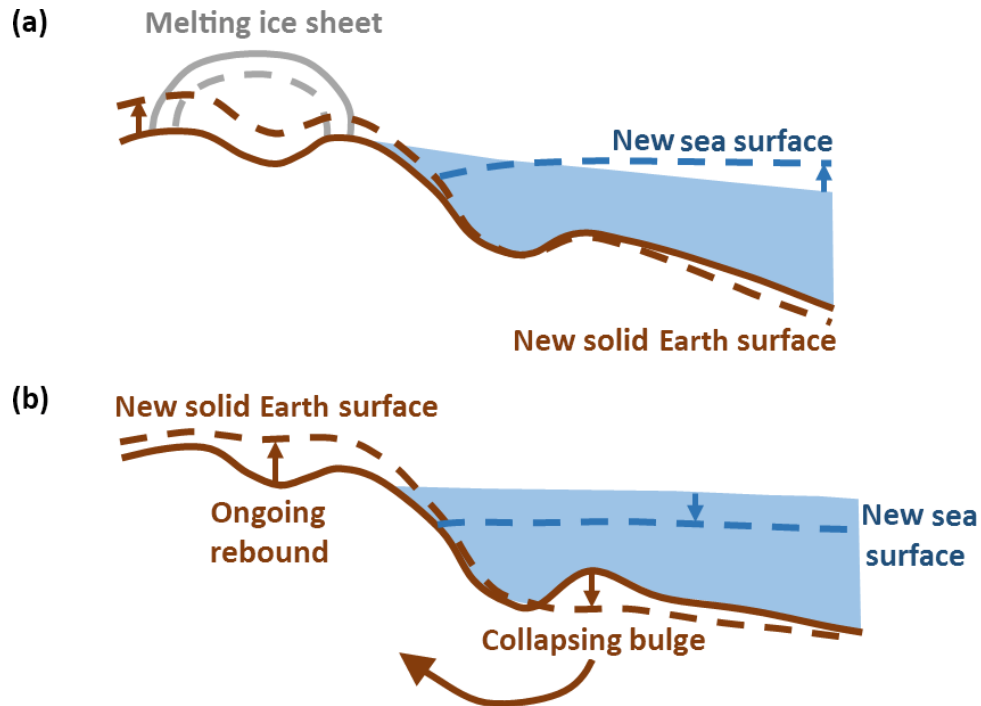
Figure 2.3: Solid Earth deformation and sea-level change. Solid lines indicate original positions; dashed lines indicate new positions. **(a)** Ice sheet masses retrieving resulting in a solid earth rebound and in a decrease in gravitational attraction from the masses. Both cause a local sea-level fall. **(b)** The solid earth relaxation is ongoing after the disappearance of the ice sheet, and a bulge outside the area collapses, thereby increasing the ocean's capacity and lowering the sea level. The figure and explanation are taken from Figure 2 in Whitehouse (2018)

During the 19th and early 20th century, the impact of GIA on observations of shoreline migration was one of the factors that shaped the ideas of climate changes, sea-level change, and isostasy.

Various sources of data are available to determine a GIA model, geological evidence to determine past ice extent, GPS measurements, and the thickness and viscosity of the lithosphere. The problems and solutions go both ways in determining some of the parameters in a GIA model. E.g. the ice extent and GPS measurements can be implemented to determine the lithosphere's thickness and viscosity.

The effects of GIA and especially PGR are experienced in Fennoscandia and North America and come respectively from the Scandinavian and Laurentide ice sheets. The effects are well surveyed in these areas and have a wealth of data to determine GIA models. The maximal land uplift in these areas is approximately 1 cm/year.

GIA also affects Greenland and the Antarctic, which is important to compensate for when using a satellite gravimetry mission that measures the whole mass variations, including the GIA effect. The GIA models computed for Greenland and Antarctica are harder to determine since they are mostly covered in ice, and there is an ongoing ice melting, affecting the measurements. It is easier to collect data in areas not covered with ice. GIA model uncertainty is consequently larger in regions presently covered by ice sheets. The GIA effect needs to be corrected in the post-processing of GRACE and GRACE-FO data, see section 3.5.3.

2.3.3 Glaciers and ice sheets

The glaciers and ice sheet variations have a huge impact on the surface geometry, orientation, and gravity field of the Earth. Its also commonly referred to as the cryosphere meaning the frozen part of the sphere.

As described above glaciers and ice sheets is one of the major force in GIA and contributes to the change in the surface geometry by its sheer weight.

The displacements of the water masses in ice sheets and glaciers can also change the orientation and rotation of the earth. The masses transmitting between being frozen and locked at one place to be a part of the water cycle or in the ocean will change the mass distribution on the Earth's surface. This can affect rotation speed, the axis and other Earth Orientation Parameters(EOP).

The weight additionally has a gravitational pull of its own, this affects nearby oceans drawing more water close and rising the local sea level. The gravitational pull from the cryosphere will be used in this study to measure the mass variations.

The glaciers also have a huge impact on the water cycle, with glaciers slowly melting during the summer season it supplies large areas with water throughout dry and drought periods.

2.3.4 Ocean and Atmospheric mass and Continental hydrology

Ocean mass is affected by tidal forces and contributes to loading. The measuring of ocean mass is a discipline with many contributions. The global sea level depends on salinity, temperature, and volume. The ocean mass also varies with seasonal and decadal rates. With GRACE it is possible to directly measure the mass change in the oceans.

Atmospheric mass contributes to loading and is affected by the tidal forces and varies globally with weather systems and seasons.

Continental hydrology contributes to loading, has a seasonal variation, and plays especially a role in areas with monsoons. It is the hydrological component in rivers, lakes, and underground.

The atmospheric and ocean mass need to be corrected in post processing see section 3.2

Chapter 3

Technology and Computational Methods

3.1 Satellite gravimetry

The main advantages of using satellites to measure gravity are that they have global coverage and give relatively long-time-series of data. One approach to determining gravity using satellites is to compare the actual orbit with the calculated and expected orbit. Therefore, any satellite launched into orbit could be used to measure the gravity field. The orbits used to be determined by the use of radio interference transmitted from the satellites or by photographing the satellites with stars as reference points. These techniques were replaced by satellite laser ranging (SLR), which uses a laser to measure the orbit. Once the Global Positioning System (GPS) became operational, it became possible globally monitor the position of other satellites. This paved the way for the CHAMP, GRACE, and GOCE which are dedicated satellite gravity missions.

3.1.1 SLR

This section is derived from Seeber (2003). The SLR technique consists of shooting laser beams at the satellites and getting return signals which give the range to the satellite. The SLR requires many SLR ground stations located all around the globe to monitor the satellite orbits effectively.

The laser beam is split in the SLR ground station, one part hits a photon detector which starts a clock, and the other is sent toward the satellite. The satellite has a retroreflector that reflects the laser beam back toward the SLR ground station. When the reflected laser beam hits a photon detector in the receiver at the SLR ground station, the clock stops. The clock is a precise atom clock, and since it's the same clock that both measures the departure time and arrival time, the method will be almost free of synchronization error.

The range of the SLR satellite to the SLR ground station can be given by:

$$r = \frac{\Delta t}{2} c$$

where r is the range, Δt is the timespan, and c is the speed of light.

The BEACON EXPLORER-B was launched in 1964 and was the first satellite to carry laser reflectors. The first successful signal returns happened the subsequent year and had an accuracy

of a few meters. In the following years to this date, the accuracy has improved and is now at sub-centimetre. It's now common to have laser reflectors mounted on the space vehicle to use the SLR technique to confirm its orbit parameters or as a backup system. Some satellite missions have also been developed and optimised to give a higher accuracy of the Earth's gravity field and orbital parameters. These are STARLETTE, STELLA, LAGEOS-1 and 2, AJISAI, ETALON-1 and 2, GFZ-1 and WESTPAC

The mains scientific fields that SLR are applied for are:

- **Gravity field and satellite orbits** SLR can precisely determine the low degree and order coefficients and precise orbit determination.

- **Positions and reference frames** SLR can give absolute geocentric coordinates and absolute height and contribute to the realisation of the International Terrestrial Reference System (ITRF)

- **Earth Orientation Parameters (EOP)** SLR can determine polar motion and variations in Earth's rotation.

The International Laser Ranging Service (ILRS) is the organisation that collects, archives and distributes the observation datasets from the 44 different SLR ground stations engaged in laser ranging.

The SLR missions are still of great value, mainly due to the accurately measured lower degrees of the spherical harmonics that have a long time series spanning multiple decades. It still contributes to the main field described above and is also combined with other space surveying techniques.

3.1.2 Dedicated satellite gravity missions

One of the main obstacles to overcome when measuring the satellite orbits is to have a uniform measurement of the positions of the satellites. This is a drawback of the SLR method, which relies on SLR ground stations that may not always have overlapping coverage. Following the establishment of Global Navigation Satellite Systems (GNSS), the orbits of other satellites can be consistently positioned using GNSS data. This has been utilised in new, dedicated satellite gravity missions based on the following three concepts:

Satelite-to-satellite tracking in high-low mode (SST-HL)

This concept is based on one satellite in low earth orbit (LEO) has its position continuously determined by GNSS satellites. The GNSS satellites are strictly in a mean earth orbit (MEO), not high earth orbit, but the term high low is kept because of the concept of different orbit heights. The satellite also has an accelerometer placed in the mass centre, which measures the perturbation forces on the satellite coming from non-gravitational forces such as solar radiation and atmospheric drag. The observed three-dimensional accelerations from the satellite correspond with the gravity accelerations. The Challenging Minisatellite Payload (CHAMP)mission used the SST-HL as its measuring technique.

Satellite-to-satellite tracking in low-low mode (SST-LL)

This concept is based on two satellites in the same LEO but separated by hundreds of kilometres. The range between the satellites is measured with the highest possible accuracy. They both use the accelerometer at their mass centre to compensate for the effects of non-gravitational forces.

The two satellites will pass over the mass anomalies at different times and will experience acceleration from the mass anomalies at different times. This means that the velocity and range will differ. The range rate is proportional to the difference in gravitational potential at the location of the two satellites. Since the SST-LL is positioned from GNSS, the SST-HL is also implied. GRACE and GRACE-FO satellite gravity missions rely on SST-LL measuring technique.

Satellite gravity gradiometry (SGG)

This concept is based on one satellite in LEO measures the acceleration difference in the satellite. It has six accelerometers on three perpendicular axes, where the origin of the axis is in the mass centre of the satellite. The measured signal is the difference in gravitational acceleration at the satellite, and the gravitational signals emanate from the masses on the Earth. This measurement technique could be compared to taking gravity gradient measurement on the Earth's surface but in three dimensions. Since the gradient is measured, the dampening effect of the satellite's altitudes is counteracted. The measured signal corresponds to the second derivative of the gravitational potential. The Gravity field and steady-state Ocean Circulation Explorer (GOCE) used SGG as its measuring technique.

3.1.3 GRACE and GRACE-FO

The GRACE and GRACE-FO missions are collaboration projects between the U.S. National Aeronautics and Space Administration (NASA) and the Deutsches Zentrum für Luft- und Raumfart (DLR).

The main goals of the GRACE mission were:

- Determination of the global high-resolution gravity field of the earth

- Temporal gravity variations

Components

The key components of the GRACE satellites are (Hofmann-Wellenhof and Moritz, 2006):

- **The K-Band Ranging system (KBR)** measures the range change between the satellites. Both satellites transmit and receive, making the measurements redundant. They transmit at two microwave frequencies to reduce ionic delay. The precision is at $1\mu\mathrm{ms}^{-1}$. The KBR is a key component of the GRACE mission.

- **The GPS receiver** gives positioning and timestamps to the satellite both for postprocessing and for the attitude control system. The postprocessing is determined on the ground through code and carrier phase range observation.

- **A Superstar Accelerometer (ACC)** mounted in the centre of mass of the satellite measures surface forces from solar radiation and atmospheric drag. Gravity forces will not affect the accelerometer as long as it is located in the centre of mass of the satellite.

- **A star camera** mounted on the satellite determines its orientation. This is used to reduce the distance measurements with KBR to the distance between the centres of mass of the satellites.

- **A retroreflector** for orbit validation using the principle described in section 3.1.1.

Measuring method

As mentioned above, GRACE and GRACE-FO use SST-LL as their measuring technique. SST-LL is explained briefly above, but a more detailed description is needed. The measurement principle is facilitated by the sketches in Figure 3.1. Satellites A and B are in the same LEO(altitude 485-500km) with a distance between them of 220 km. The orbits are almost circular and are near-polar, which is vital to get uniform global coverage.

1. In Figure 3.1.1, the velocity difference(Δv) between satellites A and B is equal to zero.

2. In Figure 3.1.2, the satellites have approached closer to a mass anomaly, and the mass anomaly is pulling more on satellite A, so it accelerates and therefore ΔV increases.

3. In Figure 3.1.3, satellite B experiences the same as Satellite A did in Figure 3.1.2, and satellite A has passed the mass anomaly, so it gets pulled in the opposite direction of its velocity and decelerates.

4. In Figure 3.1.4 satellite B experience the same deceleration as satellite A did in In Figure 3.1.3, and both satellites have the same velocity again.

GRACE-FO

The GRACE mission launched in 2002 and had a design lifetime of five years. It surpassed that and did have a 15-year successful pioneering mission. The GRACE-FO was launched in May 2018, after the decommissioning of GRACE in November 2017. The GRACE-FO mission is almost a duplicate of the GRACE mission, with the goal to continue the endeavour of tracking the mass transport in the Earth system. The GRACE-FO has a Laser Ranging Interferometer that is not used for the current mission but is tested for future satellite gravity missions. There is almost a year gap in the data between the missions. This is not ideal, but applications focusing on seasonal and long-term time scales are not greatly affected (Chen et al., 2022).

The GRACE and GRACE-FO gravity missions are great at observing temporal variations on long to medium-spatial scales and creating a potential model from one month of data.

The possibility to detect the hydrological variations through comparing multiple monthly potential models, is the reason GRACE and GRACE-FO can be used in this thesis.
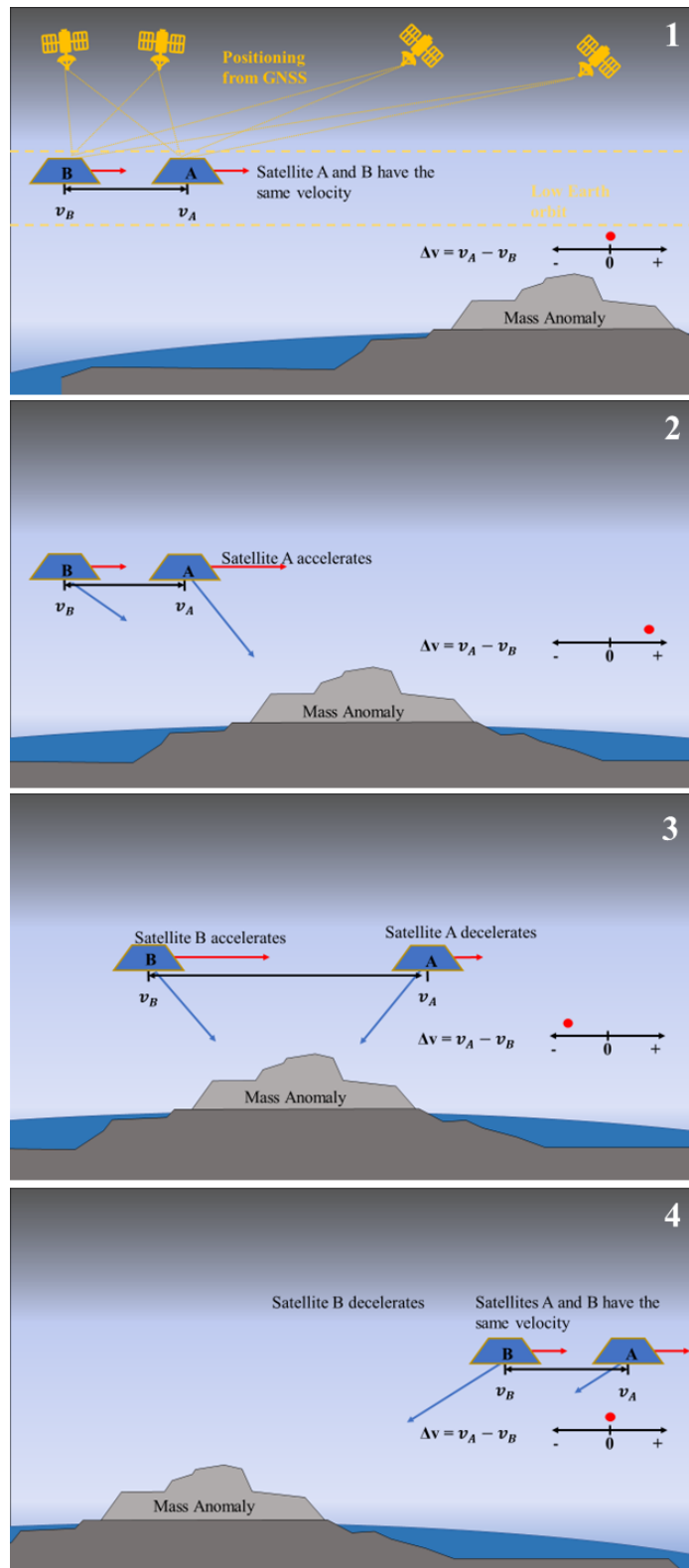
Figure 3.1: Principal diagram of GRACE and GRACE-FO measuring a mass anomaly. Figure inspired by Tapley et al. (2019)

3.2 GRACE gravity solutions

This section will look at how the GSM is derived and different approaches to the storage of the data. Solutions from the GRACE and GRACE-FO satellites are provided by three main processing centres in the Science Data System (SDS). SDS consists of the Center for Space Research at the University of Texas at Austin (CSR), NASA's Jet Propulsion Laboratory (JPL), and the German Research Centre for Geosciences (GFZ). They use the measurement from GRACE and GRACE-FO to estimate a monthly GRACE/GRACE-FO gravity solution (GSM) and distribute it on website International Centre for Global Earth Models (ICGEM) http://icgem.gfz-potsdam.de/. There are also many other calculation centers that deliver GSM through International Combination Service for Time-variable Gravity Fields (COST-G) https://cost-g.org/.

The different processing centers need to compensate for the short-term variations present in the gravity field. Tide-dependent atmospheric and ocean mass is then modeled and removed through a process called atmospheric and oceanic de-aliasing(AOD). This needs to be done before the GSM analyzed and used for mass and trend computations.

3.2.1 Processing levels

The data downloaded from the GRACE and GRACE-FO satellites are huge and need to be pre-processed before a GSM can be obtained. The following sections are derived from Wen et al. (2019) and will explain the pre-processing.

Level 0

Level-0 data: The observational raw telemetry data is downloaded for each pass and processed by the GRACE/GRACE-FO Raw Data Center (RDC) at DLR. It is separated into science instrument and housekeeping data streams.

Level 1A

Level-1 A data: Level-1 A data results from a non-destructive processing applied to the level-0 data. The level-0 data is converted from its binary encoding to science units and time-tagged by satellite receiver clock time, and quality control flags are added. The non-destructive processing means that the process is reversible to level-0. The level-1 A data also contain ancillary data products for processing to the next data level.

Level 1B

Level-1 B data: Level-1 B data is further processed from Level-1 A data. It is resampled with the correct time tag from GPS time, filtered, downsampled to a lower rate and/or converted quantities used in level 2 processing (inter-satellite range, range rate, range acceleration, and non-gravitational accelerations from both GRACE-A and GRACE-B). It also contains the ancillary data created during the process and data needed for further processing.

Level 2

Level 2 data: The level 2 data includes orbit solutions for the satellites and monthly average estimates of the Earth's gravitational potential in the form of spherical harmonics.

Level 3

Level 3 data: The Level 3 data convert the monthly gravity anomalies from Level-2 into units of surface mass anomalies and maps the data to a geographical grid. Typical liquid-water-equivalent-height.

3.2.2 Analytical methods available

The analysis of GRACE and GRACE-FO data is usually done with spherical harmonics or in spatial mascon solution(explained below). The collaborators in SDS have provided and continue to provide new releases of the solutions. For each release, the computation is improved. In this thesis Release 06(RL06) is used.

Spherical harmonics

As mentioned in the sections above spherical harmonics(SH) are one of the ways of describing a global model. The SH consists of the two potential coefficients S_{nm} and C_{nm} with its order and degree describing the global potential. When the SH is put through a spherical harmonic synthesis(SHS) we get a spatial model which shows the solution globally. The spherical harmonic coefficients are based on level 1-B data. Historically the spherical harmonic coefficients have been used in satellite geodesy, it is effective computationally, and the satellite's sensibility is implied in the harmonic basis function.

Mass concentration blocks (Mascon)

Another solution to do an analysis of GRACE and GRACE-FO data is to use the Mascon solutions. There are three concepts of mascons (Watkins et al., 2015):

- The first mascon solution is called Spherical cap mascons where the mass variations are directly decided from the range rate in level 1-B.

- The second mascon solution is similar to the first, however, each mascon basis function is represented by a finite truncated spherical harmonic expansion.

- The third mascon solution, is based on the spherical harmonic coefficients and not the range rate and is therefore not a "real" mascon. This will be referred to as a grid solution in this thesis.

The mascon solution is computed by JPL, CSR, and GFZ. It is in the spatial domain usually a matrix containing GSM with a EWH value for each pixel on the globe. The main advantage of mascon solutions is that they contain geophysical corrections and necessary replacements.

In this thesis, two mascon solutions RL06 from JPL (Wiese et al., 2023) and GSFC (Loomis et al., 2019) are used. The mascons are available through respectively https://grace.jpl.nasa.gov/data/get-data/jpl_global_mascons/ and https://earth.gsfc.nasa.gov/geo/data/grace-mascons. In these sites the processing is done to the mascons are explained, some of them can be seen in the lists under:

The JPL mascon has these data processing steps done:

- C_{20} coefficients replacement from Cheng et al. (2011).

- Geocenter correction from degree-1 coefficients replacement from Sun et al. (2016) and Swenson et al. (2008).

- GIA correction from ICE6G-D model from Peltier et al. (2015).

The GSFC mascon has these processing steps done:

- C_{20} coefficients replacement from TN-14 (Loomis et al., 2020).

- C_{30} replacement beginning August 2016 from TN-14 (Loomis et al., 2020)

- Geocenter correction from degree-1 coefficients replacement from Sun et al. (2016)

- GIA correction from ICE6G-D model from Peltier et al. (2015).

The GSFC mascon does unfortunately not contain any uncertainty measures.

3.3   Filtering of models

The GSM models derived from GRACE and GRACE-FO data are relatively noisy and show a characteristic of unphysical striping error patterns. The noise can be understood as relatively small areas with larger signals, which are not properly mapped in the solutions because of the limited spectral resolution. The stripping pattern can be interpreted as an individual realization of a noise process with spatially distinct correlation. This manifests as longitudinal stripes and is connected to the orbit geometry which is near polar. The noise and striping patterns are affecting the higher spherical harmonic degrees and therefore the more detailed part of the signal.

The process of noise-reducing filtering and retaining as many details as possible is one of the main challenges in GRACE and GRACE-FO post-processing. A lot of different filtering and noise reduction techniques have been developed. This subsection will look at a Gaussian filter and the non-isotropic DDK filter, which are the filters used in this thesis.

3.3.1   Gaussian filter

The Gaussian filter is a spatial averaging filter. This filtering method was proposed by Wahr and Molenaar (1998) and uses equations from Jekeli (1981). The weighting function W is isotropic meaning that its dependent on the distance and not the directions between the points. The normalized function is given as

$$W(\alpha) = \frac{b}{2\pi} \frac{e^{-b(1-\cos\alpha)}}{1 - e^{-2b}} \tag{3.1}$$

where

$$b = \frac{\ln(2)}{(1 - \cos(r/a))} \tag{3.2}$$

r is the averaging radius on the Earth's surface and is defined as the distance at which the convolution operator decreases to half of its maximum value $\alpha = 0$. W_n can be computed with the following recursion relations

$$
\begin{aligned}
W_0 &= \frac{1}{2\pi} \\
W_1 &= \frac{1}{2\pi}\left[\frac{1 + e^{-2b}}{1 - e^{-2b}} - \frac{1}{b}\right] \\
W_{n+1} &= -\frac{2n + 1}{b}W_n + W_{n-1}
\end{aligned}
\tag{3.3}
$$

The most common values of $r = 300$km or 500 km, according to Chen et al. (2015), and is also used in this thesis. The effects of these filters can be seen in Figure (3.3a) and (3.3b).
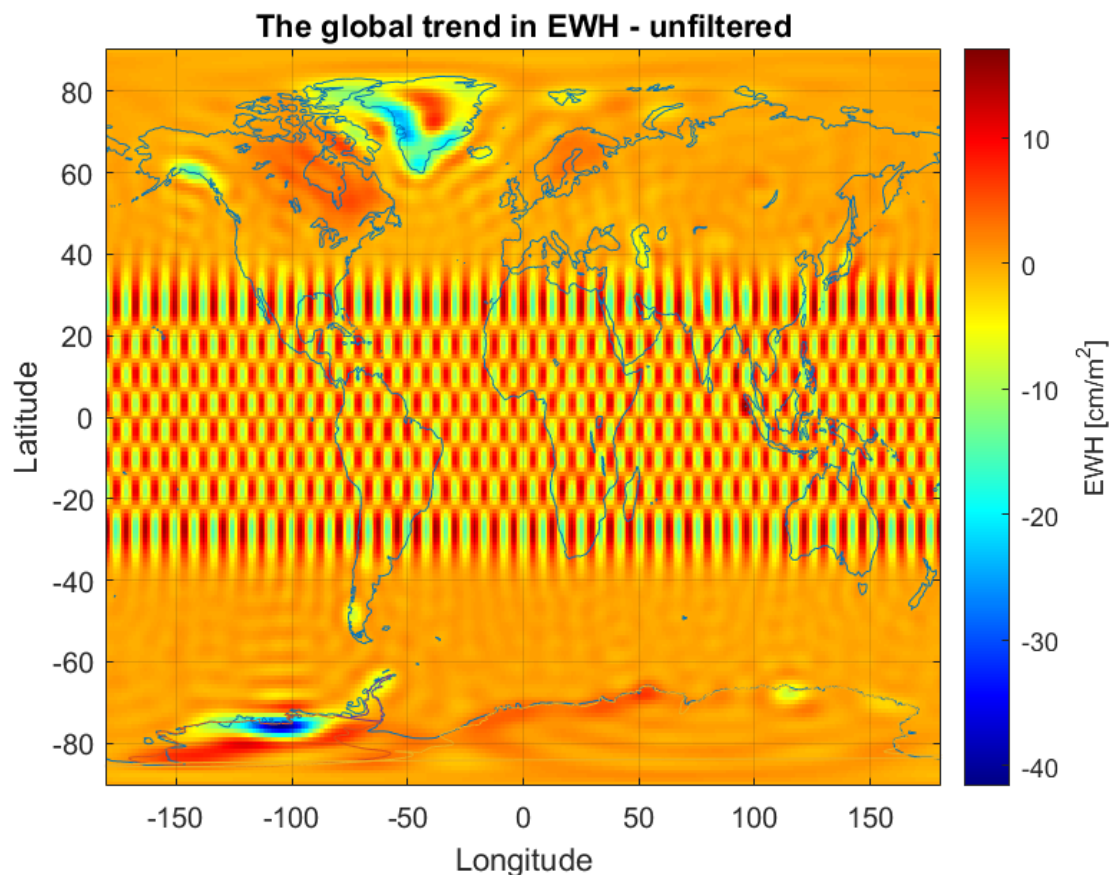
Figure 3.2: An unfiltered global trend for 2002.04-2016.08 where the longitudinal stripes are visible. An unfiltered spherical harmonic CSR RL06 solution with $L_{max} = 60$ was used to produce this global trend
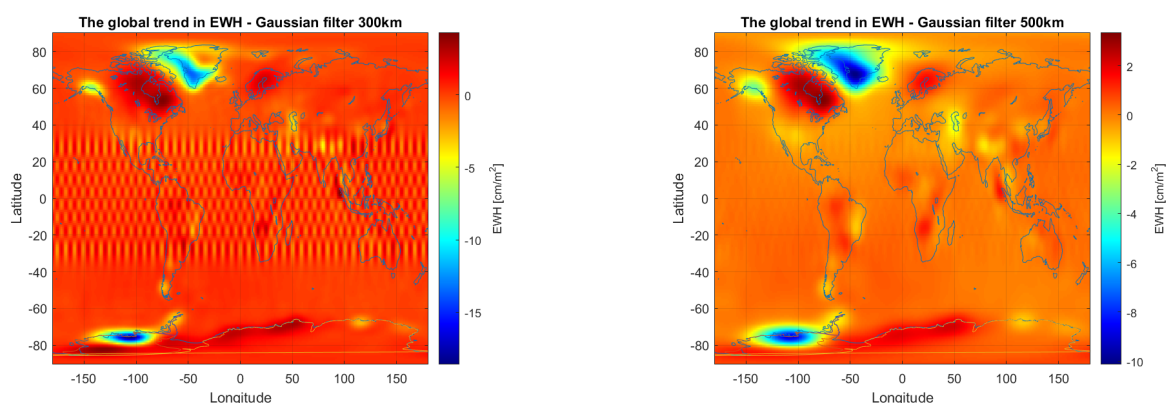
(a) The same trend 04.2002-08.2016 as in figure (3.2) but with a Gaussian filter with half response length of 300km. The longitudinal stripes are less visible but the overall signal is also dampened.

(b) The same trend 04.2002-08.2016 as in figure (3.2) but with a Gaussian filter with half response length of 500km. The longitudinal stripes are less visible but the overall signal is also dampened.

Figure 3.3: Gaussian filters for the global trend 04.2002-08.2016

27

3.3.2 DDK(non-isotropic)

A Denoising and Decorrelation Kernel(DDK) is a non-isotropic filter meaning that it is dependent on the directions to other points when filtering. The DDK filters consist of a decorrelating kernel that utilizes a synthetic error covariance matrix computed from GRACE orbits and an apriori signal covariance matrix. The signal has a correlation in the North-South direction as a consequence of the near-polar orbits. The DDK filter is counteracting this with a smoothing kernel that is tighter in the north-south direction compared to the east-west direction. The kernels are position-dependent with negative sidelobes that are dependent on the geographical latitude. The DDK filtering technique was proposed by Kusche (2007) and Kusche et al. (2009).

The DDK filters are provided solutions with DDK1-DDK8 filters by the contributers in SDS. The filters are not entirely comparable to a Gaussian filter but DDK1 DDK2 and DDK3 can correspond to an Gaussian filter with $r = 530km$, 340km, and 240km (Kusche et al., 2009).

The effect of a DDK5 filter, which is used in this thesis can be seen in Figure 3.4. It can also be compared to the Gaussian filters in Figure (3.3a) and (3.3b) where the amplitude of the signal is more dampened than with a DDK5 filter.
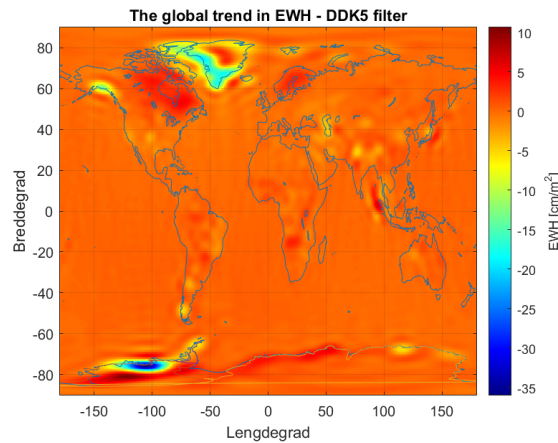
Figure 3.4: The same trend 04.2002-08.2016 as in figure (3.2) but with a DDK5 filter applied. The longitudinal stripes will be less visible.

3.4 Lower degrees replacement

The lower degrees in GRACE and GRACE-FO missions, especially the degree-2 zonal term $\Delta C_{2,0}$ show substantially large uncertainties. This can be connected to the late stages of the GRACE mission and all of the GRACE-FO mission. It is likely related to only one ACC working on one of the satellites. In GRACE one of the satellites ACC failed during the late stage, and in GRACE-FO the same happen upon launch with one of the satellites. This has resulted in large noise in the $\Delta C_{2,0}$ and $\Delta C_{3,0}$ coeffisents, which in turn results in high RMS values.

To eliminate this problem there is common to replace these coefficients with coefficients computed from SLR data. As mentioned in section 3.1.1 the lower degrees of the spherical harmonics are accurately measured with SLR and is therefore suitable to replace the more unreliable GRACE and GRACE-FO mission lower degrees. The replacements are distributed through GRACE and GRACE-FO Technical Notes. In this thesis, Technical Notes 13 and 14 were used, which utilize the SLR satellites LAGEOS-1/2, Stella, Starlette, AJISAI, Larets and LARES.

In this thesis the degree 1 is replaced from Technical Note 13 and $\Delta C_{2,0}$ where replaced from Technical Note 14 and for the GRACE-FO the $\Delta C_{3,0}$ is replaced from Technical Note 14. This is the same as presented in Loomis et al. (2021). Technical Note 13 and Technical Note 14 is available through https://podaac.jpl.nasa.gov/gravity/grace-documentation.

3.5 Mass trends of the global gravity field

3.5.1 The preparations of data

The data used in this thesis follows the method presented in Loomis et al. (2021).

As mentioned in section 3.2, the GSM is available through the website: ICGEM: http://icgem.gfz-potsdam.de/. Here it is possible to download level 2 data with spherical harmonic coefficients from GFZ, JPL, and CSR, with DDK filters from DDK1-8 and unfiltered. A text file contains a GSM with spherical harmonic coefficients for each epoch, to have it in a more suitable file format the text file is read into a matrix. The matrices are collected into a structure for the whole time series and then the lower degrees are replaced as described in section 3.4.

The drainage basins and ice sheets in Antarctica use the ice sheets proposed by Rignot et al. (2011) and is downloaded from http://imbie.org/imbie-3/drainage-basins/. Antarctica is separated into WAIS, EAIS, and AP by historical definitions in combination with ice velocity data and modern digital elevation models. AP and WAIS are divided by George VI Sound in the west to the Ronne ice shelf in the east. WAIS and EAIS are divided by the Transantarctic mountain range.

3.5.2 Different approaches of calculating trend

As mentioned in subsection Spherical harmonics (3.2.2) and subsection The preparations of data (3.5.1), each epoch has a set of potential coefficients. From the time series containing all the spherical harmonic coefficients, 4 things need to occur to obtain the mass change for each area:

1. SHS of the spherical harmonic coefficients into a grid solution

2. The areas of interest must be selected

3. Integration over the area

4. The trend must be calculated

This can happen in different orders and gives three ways of calculating the trend:

- Trend on the coefficients

- Trend on the masses for whole areas

- Trend on each pixel in an area

A schematic explanation of the three ways is given in Figure 3.5.

The selection of areas is according to the WAIS, EAIS, and AP described in section 3.5.1 and visually in Figure 1.1. Integrating an area in this thesis is done over the grid solution, where each pixel has a value given in kg/m^2. To get the masses for one area in total, each pixel value
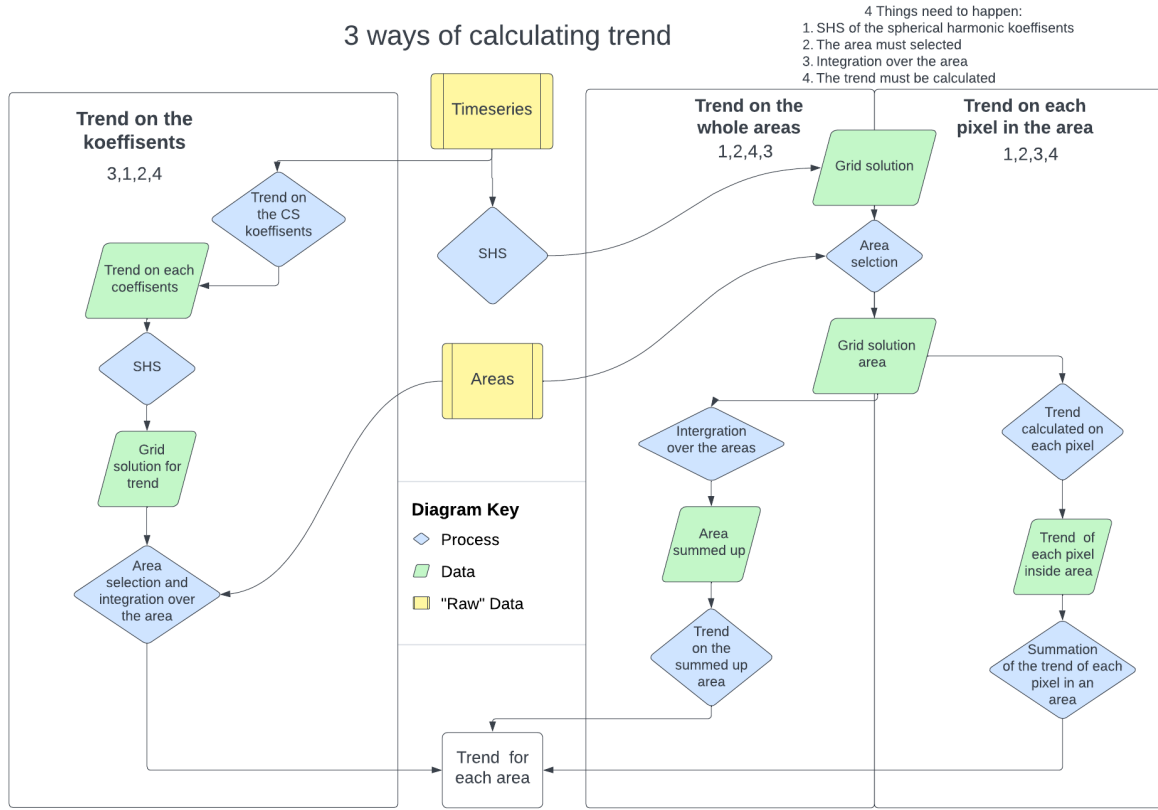
Figure 3.5: Three different approaches to calculating trend

has to be multiplied by the area of the pixel($\frac{kg}{m^2} \cdot m^2 = kg$). The area of each pixel is calculated with

$$\Delta A = r^2 \cdot sin(\theta) \cdot \Delta\theta \cdot \Delta\lambda$$

with ΔA the area of the pixel, r is the geocentric radius, θ is the co-latitude angle, $\Delta\theta$ is the width of the pixel in the latitude direction and $\Delta\lambda$ is the width of the pixel in the longitude direction.

With all these three methods the trend for each area in AIS will give almost the same trend result as shown in Table 3.1. As visible there are some differences between the computations, this can be explained by the different ways the uncertainties of the model are implemented. The trend on the uncertainty measure for each coefficient is used for the weighting for the epoch, however, with a trend on the whole area and on each pixel in each area the uncertainty measure is transformed into a grid solution. For each pixel in each area, this uncertainty measure is used to weigh each epoch of the trend. For the trend on whole areas, the uncertainty measure is integrated for the whole area and gives the uncertainty of mass in each epoch which is used for weighing.

In the computations done in this thesis to obtain trends, the trend on coefficients and the trend on whole areas will be used. However, the results shown in Table 3.1 is not entirely correct. Because of leakage (see section 3.6) and GIA (see section 3.5.3) there are still some corrections necessary to obtain correct mass trends.

Table 3.1: Three different ways of calculating trend with time series 04.2002-08.2016, DDK5 solution.

Results	WAIS	EAIS	AP	Total AIS
Trend on coefficients	-41.02	68.56	-2.66	24.87
Trend on whole areas	-41.47	68.63	-2.70	24.45
Trend on each pixel in each area	-41.47	68.63	-2.69	24.46

3.5.3 GIA-models

There are numerous GIA models available. In this thesis, three global GIA models have been chosen to examine. The GIA model developed in Caron et al. (2018), Sun and Riva (2020) and the ICE6G-C from Peltier et al. (2015) will be analyzed in this section.

As mentioned in section 2.3.2, a GIA model can be determined from different data; past ice extent, GPS measurements of vertical motion, vast leveling networks, relative sea-level (RSL) data, gravity measurements, thickness, viscosity, and density of the lithosphere. What type of measurements, how they are weighted, and where on the globe measurements are obtained, are what differentiate different GIA models. All the different ways to establish GIA models make the solutions ambiguous and this leads to the GIA modeling a complex field of study.

Historically GIA models have been created with the intent to examine past ice ages and their effects on the sea level and past earth rotation. They have been established with geological evidence of past ice extent, reconstruction of past sea levels, and observation of Earth's rotation. These GIA models are not that great for corrections for GRACE effects since they lack both spatially global and temporal observations.

When establishing GIA models which better describe the effects experienced in the present time, geodetic observations of land uplift or subsidence are included. This is the method the model from Caron et al. (2018) and ICE6G-C model from Peltier et al. (2015) utilizes.

The model from Caron et al. (2018) uses 11,451 RSL and 459 GPS data, ice sheet history, and lithosphere models. The measurements come from numerous studies and are spread globally but mainly in the areas expected to experience GIA effects, North America, North Europa (especially around the Baltic Sea), and Antarctica which is dominated by GPS measurements. The model from Caron et al. (2018) is provided with formal errors, which is established through Bayesian methods and large test of different GIA models.

The ICE6G-C model from Peltier et al. (2015) is a combination of RSL, GPS, and lithosphere viscosity models. It uses large series of RLS data and GPS data.

The model from Sun and Riva (2020) is "semi-empirical" meaning that it combines GRACE data and physical basis functions. The "semi-empirical" term is applied due to the implementation of GIA "fingerprints" based on the same physics as classical forward models, but with gravity change measurements that are updated without making changes to estimates of past ice coverage or mantle viscosity.

The GIA effect in the AIS is hard to compute. The reasons are that the topography models for the land masses underneath the ice sheet are still being improved, there are few places available to do sea-level measurements, GPS measurements are possible however in a hard environment

without any infrastructure disabling the possibility of long time series, and the ice-sheet past extent is hard to uncover since the continent is still covered in ice.

GIA trends in AIS from Caron et al. (2018), Sun and Riva (2020) and ICE6G-C from Peltier et al. (2015)

The models were downloaded as spherical harmonic models. The model from Caron et al. (2018) has a spherical harmonic degree of 90, the model from Sun and Riva (2020) has a spherical harmonic degree of 60 and the ICE6G-C from Peltier et al. (2015) has a spherical harmonic degree of 256. In this thesis and comparisons all the models were chosen with a spherical harmonic degree of 60. The solutions were then integrated over for each AIS area to find its effect on that area on a yearly basis. This is presented in Table 3.2, 3.3, and 3.4 with three different spatial resolutions. The pixels selected for the summation depend on the spatial resolution and it is expected to be more accurate with a higher spatial resolution. This is seen in the column for AP which increases its trend for higher resolution and this is likely because of AP's relatively thin area. The GIA models are visualized globally in Figure 3.6 and for AIS in Figure 3.7

When the different models are compared, the model from Sun et al. (2016) differs and has smaller amplitudes than Caron et al. (2018) ICE6G-C from Peltier et al. (2015). Sun et al. (2016) uses only GRACE to compute its GIA model, in contrast to Caron et al. (2018) ICE6G-C Peltier et al. (2015) which has GPS measurements from AIS.

ICE6G-C was chosen to use further in this thesis for corrections, it is used in Loomis et al. (2021) and the mascon solutions used in this thesis utilize an ICE-6G-D model.

Table 3.2: The GIA mass trend pr year in AIS computed with Caron et al. (2018). Solutions are in different spatial resolutions. All units are in Gtonn/year.

Regions	WAIS	EAIS	AP	Total AIS
Res = 3°	30	30	2	72
Res = 1°	27	41	4	72
Res = 0,5°	28	41	4	72

Table 3.3: The GIA mass trend pr year in AIS computed with Sun and Riva (2020). Solutions are in different spatial resolutions. All units are in Gtonn/year.

Regions	WAIS	EAIS	AP	Total AIS
Res = 3°	23	33	2	57
Res = 1°	21	33	3	57
Res = 0,5°	21	34	3	57

Table 3.4: The GIA mass trend pr year in AIS computed with ICE6G-C from Peltier et al. (2015). Solutions are in different spatial resolutions. All units are in Gtonn/year.

Regions	WAIS	EAIS	AP	Total AIS
Res = 3°	48	25	2	75
Res = 1°	44	27	4	76
Res = 0,5°	45	28	4	77
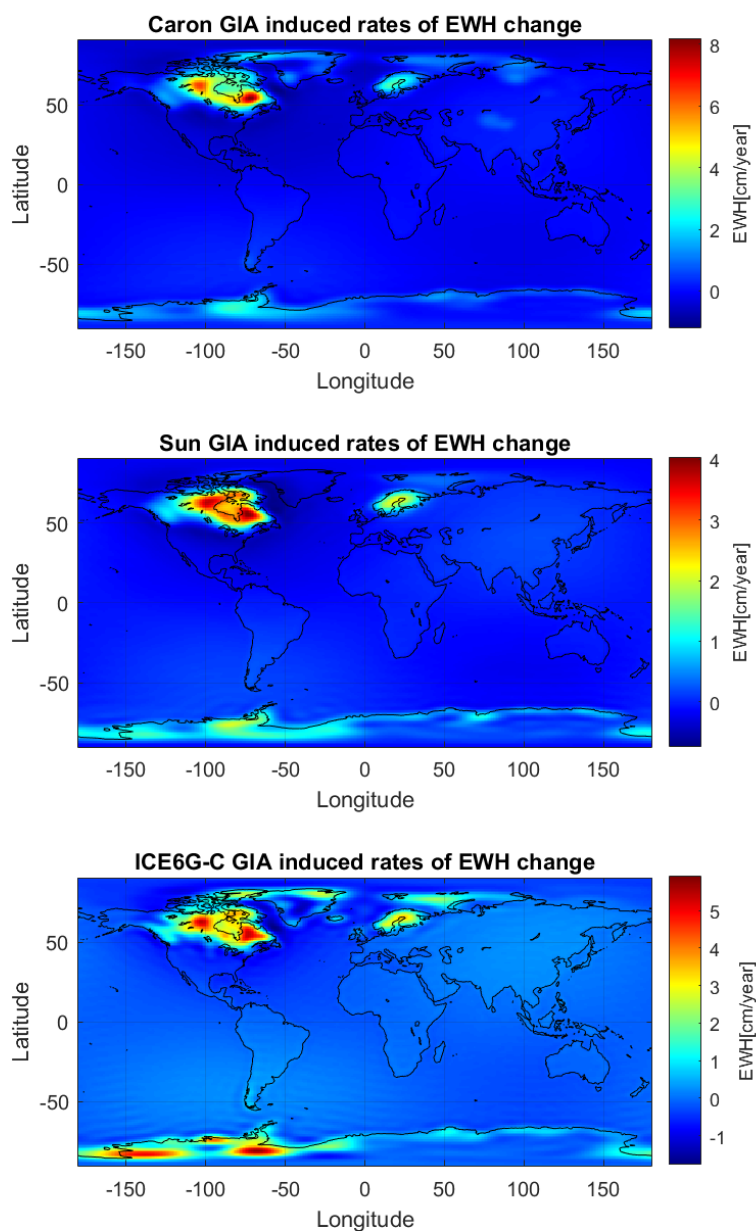
Figure 3.6: Global visualization of the three GIA models from Caron et al. (2018), Sun and Riva (2020), and ICE6G-C from Peltier et al. (2015). Notice that the color scale is different for each model

Uncertainties for the GIA models

The spherical harmonic coefficients downloaded from Sun and Riva (2020) and ICE6G-C from Peltier et al. (2015) did not include any uncertainty measurements. To find a measure of the uncertainties for the ICE6-G model for this thesis the standard deviation between the three model estimates is performed. Which can be seen in Table 3.5.

33
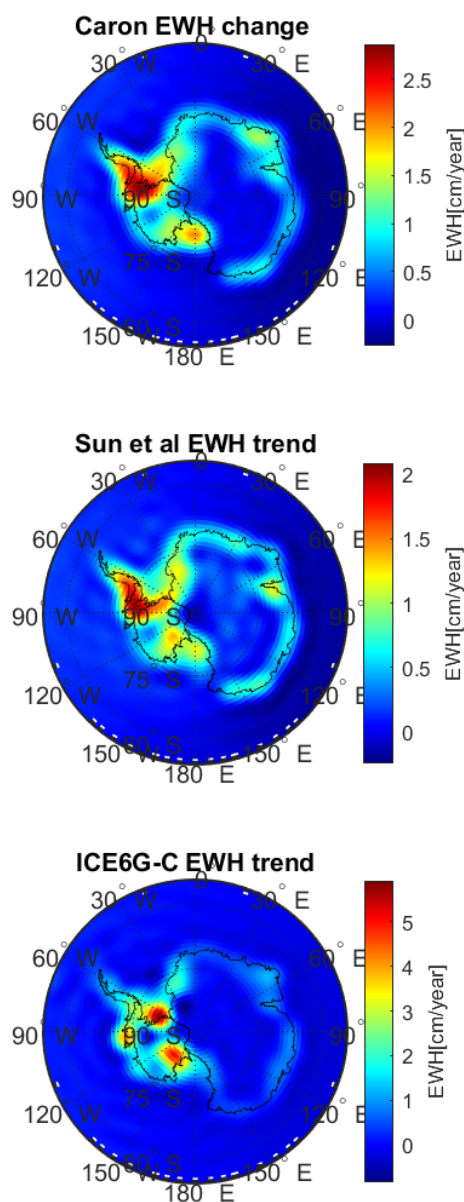
Figure 3.7: Polar stereo-graphic visualization of the three GIA models from Caron et al. (2018), Sun and Riva (2020), and ICE6G-C from Peltier et al. (2015). Notice that the color scale is different for each model

Table 3.5: The standard deviation computed of the GIA models mass trend estimates in Table 3.2, 3.3 and 3.4. The uncertainties are in different spatial resolutions. All units are in Gtonn/year.

Regions	WAIS	EAIS	AP	Total AIS
Res = 3°	17,2	15,1	0,9	30,4
Res = 1°	15,9	15,4	1,6	30,4
Res = 0,5°	16,2	15,5	1,6	30,8

3.6 Leakage

The leakage effect occurs because of the limited spectral resolution and the spatial averaging of the signal. Spectral leakage occurs when high-frequency signals are wrongfully propagated onto the lower-frequency signals, which gives an artificial signal. The limited spectral resolution is due to the GRACE solutions being limited to a maximum spherical harmonic degree of 60 or 96. These limitations will in a spatial resolution be respectively approximately 333 km and 208 km. In this thesis, a spherical harmonic degree of 60 was chosen as Loomis et al. (2021) did and noted that degree 96 produced more unrealistic anomalies in the global trend. The spherical harmonic signals would need to go to infinity to convey a perfect representation of the signal with accuracy as detailed as the real world.

In the spatial domain, the signals appear to be spread spatially from an area with significant mass change to surrounding areas. This can be further propagated by spatial averaging filters. Theoretically, a detailed signal will be spread all over the globe, however with diminishing signal strength as the distance from the origin increase.

For a visual context Figure 3.9.d shows the leakage spatially from a constructed signal in Figure 3.9.a.

The leakage can be split into two contributions; leakage into and leakage out of the area of interest. The leakage into the area could contribute to a higher amplitude of the signal than is real. In Antarctica, it could be that the different areas, WAIS, EAIS, and AP, get a contribution from one of the other areas. It is of interest to find the signals leaking in and reducing it. The leakage out would attenuate the signal and spread it to the surrounding areas. It is of great interest to find and revert the effect.

Since AIS is a continent, the leakage into it is low and, in this thesis, not looked at. The leakage out of AIS to surrounding ocean areas is of a larger magnitude and will be further looked at.

The leakage effect would affect the estimation of the mass change. The mass change could be overestimations or underestimations compared to the actual mass change, depending on which area that is of interest.

3.6.1 Forward modeling

One of the suggestions to compute and subtract the leakage effect is an iterative forward modeling (FM) algorithm proposed by Chen et al. (2015). The idea is to find a mass rate model that represents the true mass rates. The iteration is described schematic in Figure (3.8)

The iteration technique starts with an initial model, it could be the observed data, or it could be a constructed signal to test the effect of the FM.

If there is a constructed signal, it is first sent through an SHA which utilizes the equation (2.31) to compute spherical harmonic coefficients. They are selected to be up to a degree and order to describe the signal, usually degree and order 60. An SHS that uses equation (2.30) implementing the spherical harmonic coefficients and computes a prediction of the constructed signal. This prediction will almost be what we could expect GRACE to observe. The prediction will not be the same as the computed signal since SHA truncates the signal by a limited spherical harmonic degree, and SHS can have a Gaussian filter applied, which further diminishes the signal.

This observation is then taken into an iterative loop, and a model is based on the observation. The goal of the iteration is to reconstruct the constructed signal, or with real observations,

reconstruct the real signal expected to be in the area. Now the signals from the model will be selected by the area and only the signals inside the area will be used in the SHA. This creates spherical harmonic coefficients, which are again used in SHS to compute a prediction.

The predicted signal will then be compared against the observed signal and make the difference ΔM. The model is then adjusted by ΔM with an iteration factor k. The model is then again set through an SHA and SHS, and the iterations continue.

The loop iterates until either the mass of ΔM is lower than a pre-set value (eg. 1% of the mass of M_{obs} or when a set of iterations has been done.

When the iterations are completed, the model is returned. The area iterated over has the signal corrected for leakage. If the iteration is done one more time, and computed a prediction one more time, the areas outside the iteration area selected will be leakage out signals from the reconstructed signals. The iteration area in thesis will be the AIS area.

In this thesis, it is tried to replicate some of the results from Chen et al. (2015) to check if the FM developed in this thesis works. The constraints of areas for the construction of the signal
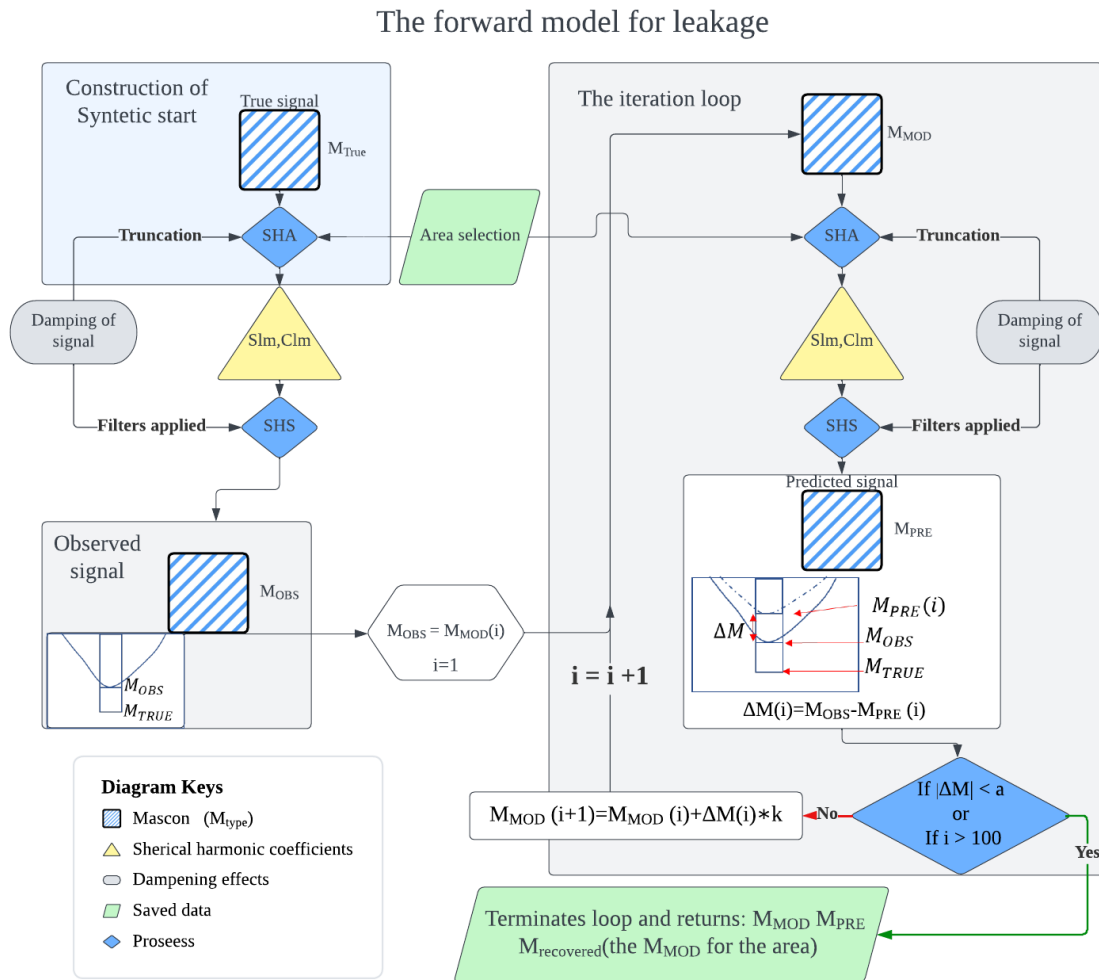

Figure 3.8: A schematic visualisation of the Forward model

were hard to fully replicate. Instead, an approximation of the areas of the constructed signal was used. To validate, the constructed signal was subtracted from the reconstructed signal and the difference is the same order of magnitude as the same differentials in Chen et al. (2015). The spatial patterns show to have similar behavior in this thesis and in Chen et al. (2015). Some of the results from the testing in this thesis are shown in Figure 3.9 and can be compared to Figures 3 and 6 in Chen et al. (2015).

One of the aspects from Chen et al. (2015) which is not implemented in this thesis is the adjustment to conserve total water mass. In Chen et al. (2015) a uniform layer of water is placed in the global oceans to adjust for when the land mass changes. This may affect how well the FM made in this thesis perform, compared to the one proposed in Chen et al. (2015).
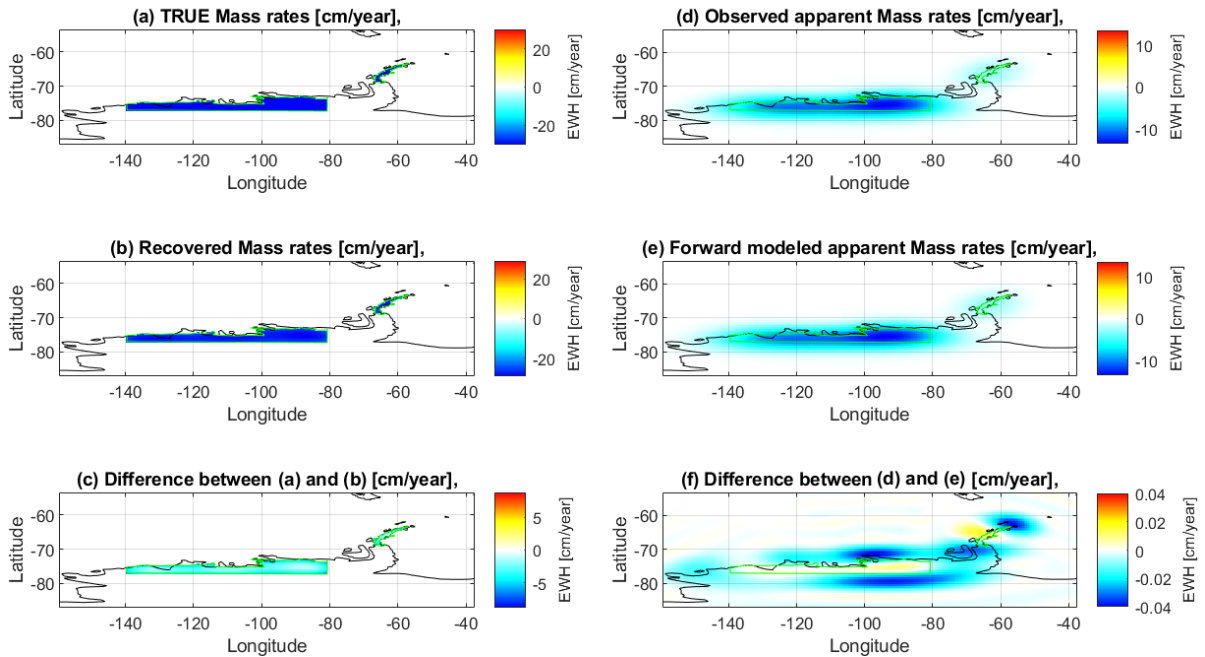
Figure 3.9: FM with a Gaussian filter with half response length of 300km and spherical harmonic degree at 60 and with 100 iterations. The green line represents the area of the FM iterates over and the constructed signal is based on. **(a)** The constructed true mass rates where the observation derive from; **(b)** The recovered mass rates after the FM is complete; **(c)** The difference between the constructed mass rate signal and the recovered mass rate signal; **(d)** Observed apparent mass rates deriving from SHA and SHS of the constructed true mass rates (a); **(e)** the apparent masses derived from the recovered mass rates (b); **(f)** The difference between the observed apparent mass rates and the apparent mass rates derived from the FM. This figure was inspired by Figures 3 and 6 in Chen et al. (2015)

Chapter 4

Results

In this chapter, a proof of concept will be presented and compared to the reference literature and mascon solutions. The GRACE-FO data will be included and a trend from 04.2002 til 11.2022 will be computed. The same time series will be divided to understand how the trend is changing.

4.1 Proof of concept

4.1.1 The approach by Loomis et al.(2021)

Loomis et al. (2021) looked at a time series from 04.2002 to 08.2016 and, used the RL06 of CSR with a DDK5 filter. They used spherical harmonic coefficients up to Nmax = 60. Each monthly solution had its degree 1 replaced by the values found in GFO technical note 13 and it's C_{20} from GFO technical note 14. The ICE-6G model was used to compensate for the GIA effect. To correct for seismic activity in this time series, they removed the three earthquakes: 2004 Sumatra-Andaman, 2010 Maule, and 2011 Tohoku-Oki. They computed their uncertainties by comparing and validating them with the high-quality GOCO-06S satellite-only global gravity field model (Kvas et al., 2021).

The mass trends presented in Loomis et al. (2021) are presented in Table 4.1.

Table 4.1: The mass trends computed with time series 04.2002-08.2016 as shown in Table 2. in Loomis et al. (2021), the GRACE part of the signal reconstructed from the total and GIA signal. All units are in Gt/year.

Loomis et al 2021	WAIS	Std	EAIS	Std	AP	Std	Total AIS	Std
GRACE(Total & GIA-derived)	-116	23	89	15	-30	10	-57	29
GIA	32	14	20	25	4	2	56	26
Total	-148	27	69	29	-34	10	-113	39

4.1.2 Computation results

The trend was calculated with different spatial resolutions in Table 4.2, 4.3 and 4.4. The trend and uncertainties for the ICE6G-C GIA model are computed in section 3.5.3. The uncertainties for the mass estimates are computed with the uncertainty measures given to each coefficient and give the formal error of the mass trends. This is not directly comparable to the uncertainties presented in Loomis et al. (2021) which are empirical errors, since it compares it with high-quality GOCO-06S satellite-only global gravity field model (Kvas et al., 2021).

When comparing the mass trend estimates in Table 4.2, 4.3 and 4.4 with each other, none of the trends significantly differ from each other except the Mass estimate Res = 3° AP which significant different from Res = 1°, and Res = 0.5°. This may be of the broad spatial resolution and the relatively small area of the AP. The comparison is between the GRACE-derived mass estimates when the GIA correction is applied the relatively large uncertainties from the GIA models follow and it is hard to get any significantly different results.

The mass trends in this thesis in Table 4.2, 4.3 and 4.4 do not significantly deviate from the mass trends in Loomis et al. (2021) seen in Table 4.1

The spatial resolution in Table 4.2, 4.3 and 4.4 varies with respectively 3°, 1° and 0.5°. The spatial resolution will affect the coastal areas the most, with higher resolution there will be a better distinction between the signals inside and outside the areas. Although this means that Table 4.4 with a spatial resolution of 0.5° should give the most precise mass estimates, it seems like Table 4.3 with a spatial resolution of 1° fits best with the mass trends from Loomis et al. (2021) in Table 4.1. It could be that Loomis et al. (2021) uses the same spatial resolution. However, the difference for total AIS is between Table 4.1 from Loomis et al. (2021) and in this thesis is for: Res =1 ° 31,01 Gt/year (Table 4.3) and Res = 3° 31,14 (Table 4.4), which is not significant.

In this thesis the trend estimates are tested if they are significantly different with a t-test:

$$t = \frac{(Trend_1 - Trend_2)}{\sqrt{std(Trend_1)^2 + std(Trend_2)^2}}$$

If the t value is larger than the t-table value the estimates significantly differ. The t-table values were obtained with a 5% significance level.

Table 4.2: Mass estimates trends computed with time series 04.2002-08.2016 after FM corrections (100 iterations) with resolution on 3°. All units are in Gt/year.

Regions	WAIS	Std	EAIS	Std	AP	Std	Total AIS	Std
Mass estimates Res = 3°	-98	2	102	4	-21	1	-17	4
GIA from ICE6G	48	17	25	15	2	1	76	30
Total	-146	17	77	16	-23	1	-92	31

Table 4.3: Mass estimates trends computed with time series 04.2002-08.2016 after FM corrections (100 iterations) with resolution on 1 °. All units are in Gt/year.

Regions	WAIS	Std	EAIS	Std	AP	Std	Total AIS	Std
Mass estimates Res = 1°	-100	2	101	4	-27	1	-26	4
GIA from ICE6G	44	16	27	15	4	2	76	30
Total	-144	16	74	16	-32	2	-102	31

Table 4.4: Mass estimates trends computed with time series 04.2002-08.2016 after FM corrections (100 iterations) with resolution on 0.5°.All units are in Gt/year.

Regions	WAIS	Std	EAIS	Std	AP	Std	Total AIS	Std
Mass estimates Res = 0.5°	-100	2	101	2	-27	1	-26	4
GIA from ICE6G	45	16	28	16	4	2	77	31
Total	-145	16	73	16	-31	2	-103	31

The trend for AIS is presented spatially in Figure 4.1. The trend for WAIS and AP is presented spatially in Figure 4.2. In these figures it is clearly visible that the FM improves the mass estimates in AIS. The trends in WAIS and AP are of special interest, the largest part of the signal that represents the mass loss in AIS are in WAIS and AP.
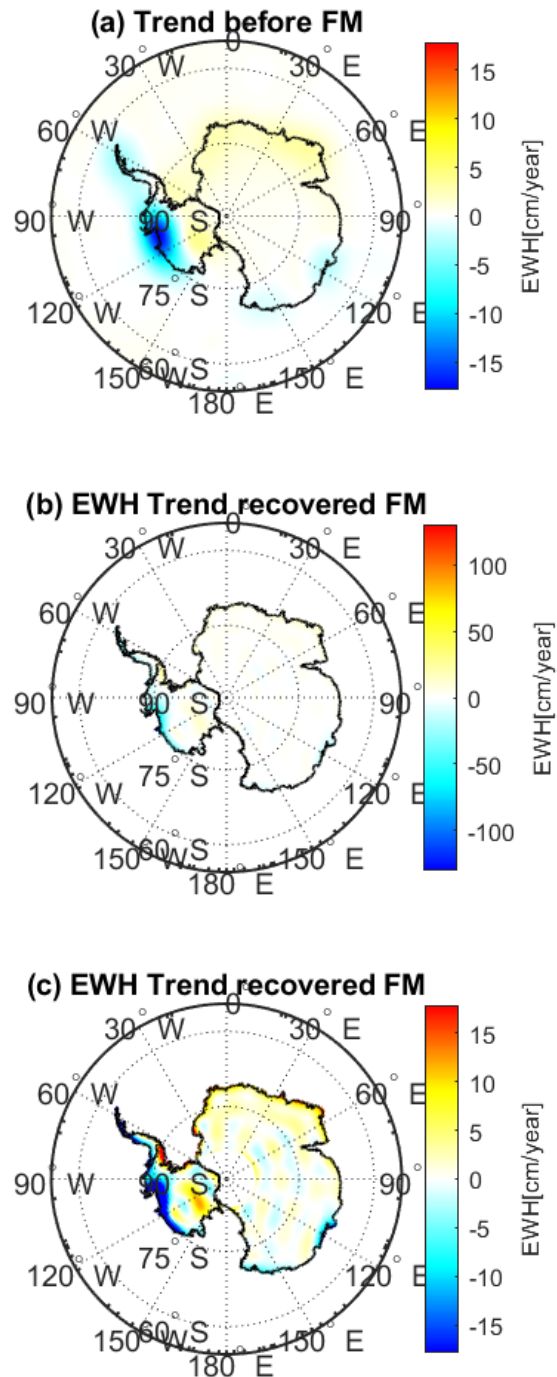
Figure 4.1: The trend in AIS with a spatial resolution of 0.5°, **(a)** The trend before FM correction; **(b)** after the FM correction with a color scale similar to the maximum and minimum values in the AIS area; **(c)** after the FM correction with a color scale similar to (a)

Figure 4.2: The trend in AIS focus on WAIS and AP, with a spatial resolution of 0,5°. **(a)** The trend before FM correction; **(b)** after the FM correction with a color scale similar to the maximum and minimum values in the AIS area; **(c)** after the FM correction with a color scale similar to (a)
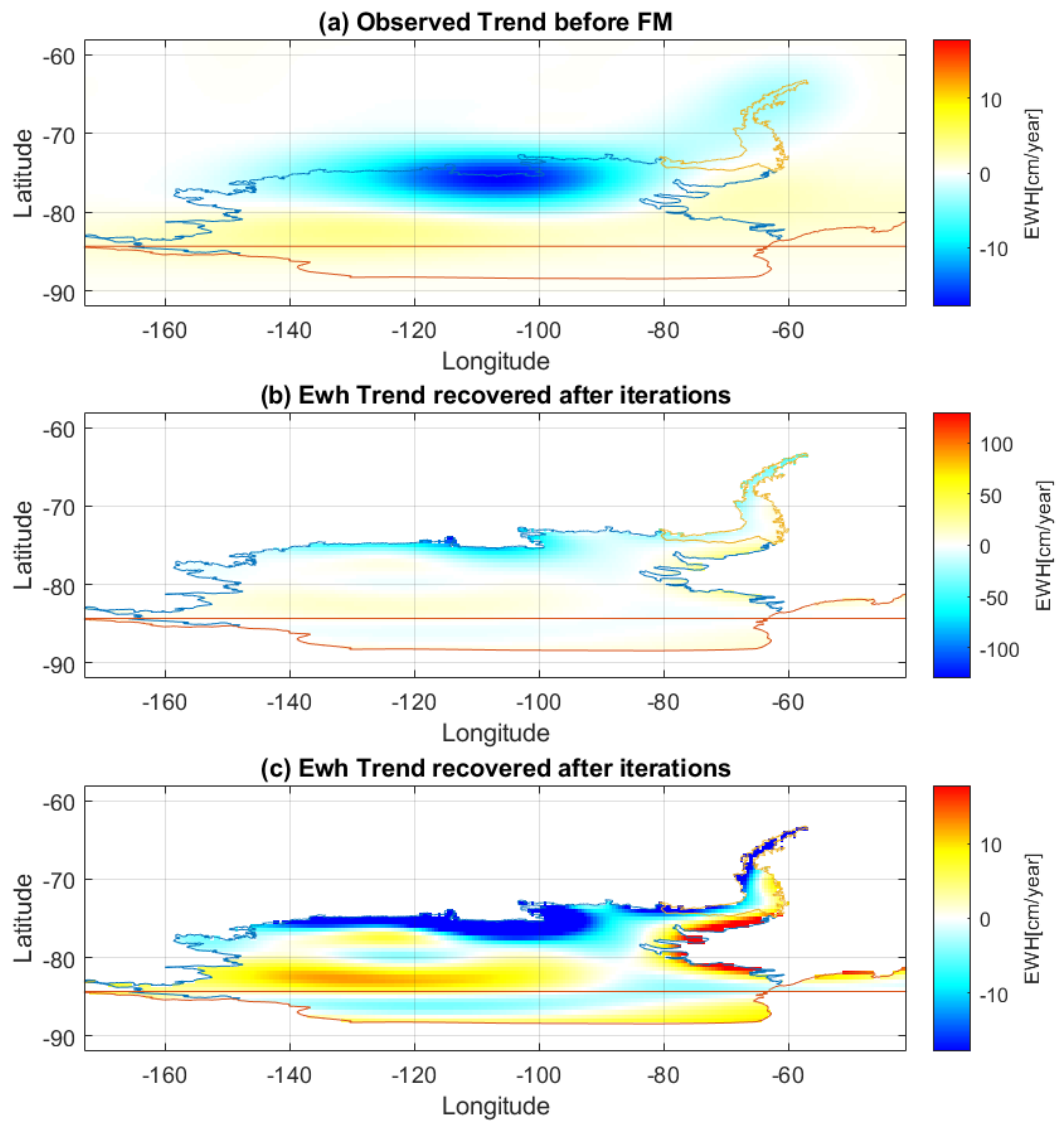
4.1.3 Mascon solutions

In Table 4.5 the trends computed from the time-series 04.2002-08.2016 for WAIS, EAIS, and AP are computed through the MASCON with 0.5° pixels from GSFC and JPL. The mascons are when downloaded already compensated for GIA effects. The computation technique here is the trend computed of the masses for whole areas, as described above in section 3.5.2. The standard deviation presented in Table 4.5 is a formal error from the trend fitting with the variance factor. Therefore the GIA uncertainty which is expected to be an order of magnitude larger is not included, and the uncertainty can be considered to be rather optimistic.

The GSFC trends presented in Table 4.5 are not significantly different from the WAIS and EAIS and Total AIS trend presented in Table 4.4 (spatial resolution 0.5°), however, AP is significantly different. When compared to the results from Loomis et al. (2021) in Table 4.1 all the trends are not significantly the different. The same applies to the JPL mass trends presented in Table 4.5.

Table 4.5: The trends computed with the time series 04.2002-08.2016 from MASCON solutions from GSFC and JPL. All units are in Gt/year. Std computed through the mass variations

Regions	WAIS	Std	EAIS	Std	AP	Std	Total AIS	Std
GSFC corrected for GIA	-128	2	58	3	-19	0	89	3
JPL corrected for GIA	-141	3	65	2	-19	0	-95	3

A visualization of the mass trend and variations computed from mascon from JPL and GSFC can be seen in Figure 4.3 and 4.4.
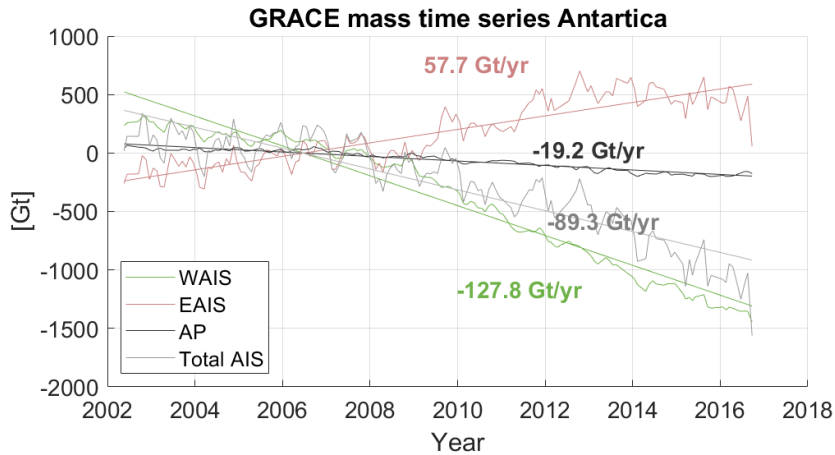

Figure 4.3: The mass trend and variations derived from the GSFC mascon for 04.2002-08.2016.

4.2 Inclusion of GRACE-FO data

The GRACE-FO gravity mission is still operative and new GSM have been released by the collaborators in SDS up until the end of 2022 when the computations in this thesis was done. The goal of this section is to look at the trend and see if it is accelerating or decelerating. It would be looked at through two larger time series and 6 smaller time spans. These trends have not been compared to the literature, no literature where the same time series was used was found. In this section, the spatial resolution of the solutions computed is reduced to only 1 ° solutions, because the FM is computationally intensive when applied to each epoch of
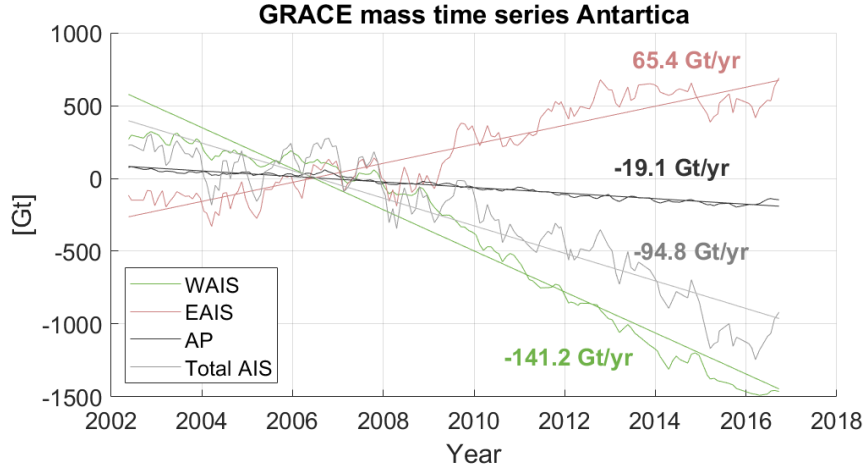
Figure 4.4: The mass trend and variations derived from the JPL mascon for 04.2002-08.2016.

GSM. When the GRACE-FO data is included the C_{30} coefficient is also replaced with C_{30} from technical note 14. This replacement is described in Loomis et al. (2021).

4.2.1 Trend calculated from coefficients

The trends calculated from coefficients with FM can be seen in Table 4.6.

Table 4.6: Mass estimates trends computed with the time series 04.2002-11.2022 after FM corrections (100 iterations) with a spatial resolution on 1 °, trend computation on the coefficients. All units are in Gt/year.

Regions	WAIS	Std	EAIS	Std	AP	Std	Total AIS	Std
Mass estimates with Res = 1°	-99	1	88	2	-18	0	-29	3
GIA from ICE6G-C	44	16	27	15	4	2	76	30
Total	-143	16	61	16	-23	2	-105	31

When comparing the GFO-included trends from Table 4.6 with the time span from Loomis et al. (2021) trend Table 4.3, WAIS, EAIS, and the Total AIS are not significantly different, but AP differ significantly. The difference in the trends between the time period 04.2002-04.2016 and 04.2002-08.2016 is for WAIS 3,6 Gt/year, EAIS -2,4 Gt/year, AP 9,7 and Total AIS 10,9. This means that the trend seems to decelerate in WAIS, AP and the total AIS, however for EAIS the positive trend seems to decelerate.

4.2.2 Trend calculated from FM on each epoch of GSM

In this section, the results of running an FM on each epoch of GSM and then calculating the trend are shown. The FM was run with the break condition when the masses of ΔM in AIS was 1% of the masses of M_{obs} in AIS. The main motivation to run an FM on each epoch of GSM is to plot the mass variances to get a visual deception of the development of the masses. All the figures in this section have been corrected for GIA in an effort to see the impact the mass changes in AIS have on the global sea level. To calculate the sea-level change seen in the figures, it is assumed that 1 mm global mean sea level change = -362Gt as stated in Sun and Riva (2020). This also coincides with the findings in this thesis. The ocean area was computed with a landmask file from JPL to be $36,33 \cdot 10^9$ km². When the 362 Gt is divided by this area it results in 1mm.

The first computations presented in Table 4.7 and Figures 4.5, 4.6, 4.7, 4.8, and 4.9 were done with FM on each GSM solution as they were containing the normal field. After the FM was run on each epoch, the mass was integrated over each area and then differing from the first epoch to find the trend.

Table 4.7: FM computed on each epoch of GSM solution, with cutoff when $|\Delta M|=1\%$ of $|M_{obs}|$, differing mass estimates after FM. Trend computed with the time series 04.2002-11.2022. All units are in Gt/year.

Regions	WAIS	Std	EAIS	Std	AP	Std	Total AIS	Std
Mass estimates with Res = 1°	-135	1	96	2	-22	0	-62	3
GIA - ICE6G-C	44	16	27	15	4	2	76	30
Total	-179	16	69	16	-26	2	-137	31

Figure 4.5: Mass variations and trend for WAIS computed with FM run on each epoch of GSM solution, with cutoff when $|\Delta M|=1\%$ of $|M_{obs}|$, differing mass estimates after FM. Trend computed with the time series 04.2002-11.2022.
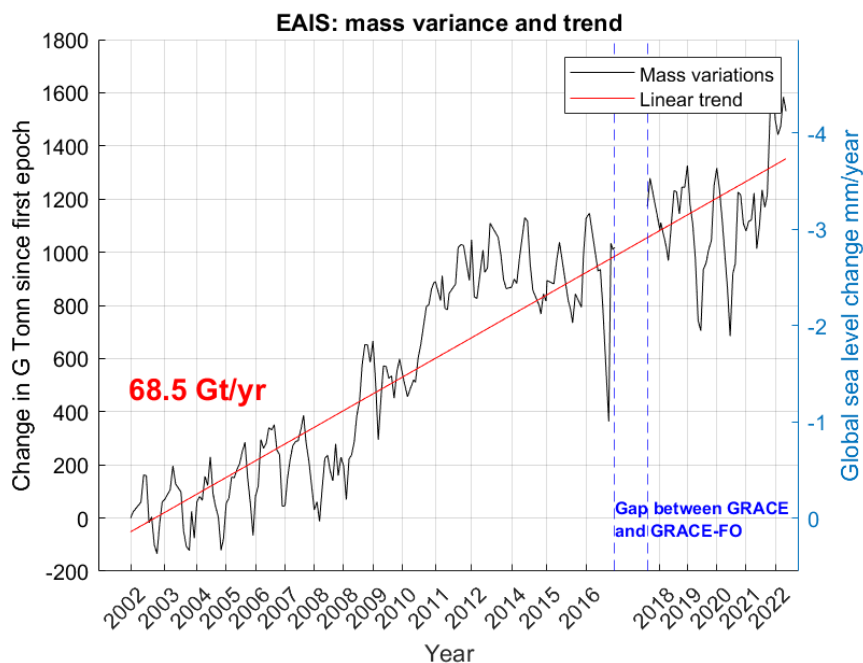
Figure 4.6: Mass variations and trend for EAIS computed with FM run on each epoch of GSM solution, with cutoff when $|\Delta M|=1\%$ of $|M_{obs}|$, differing mass estimates after FM. Trend computed with the time series 04.2002-11.2022.
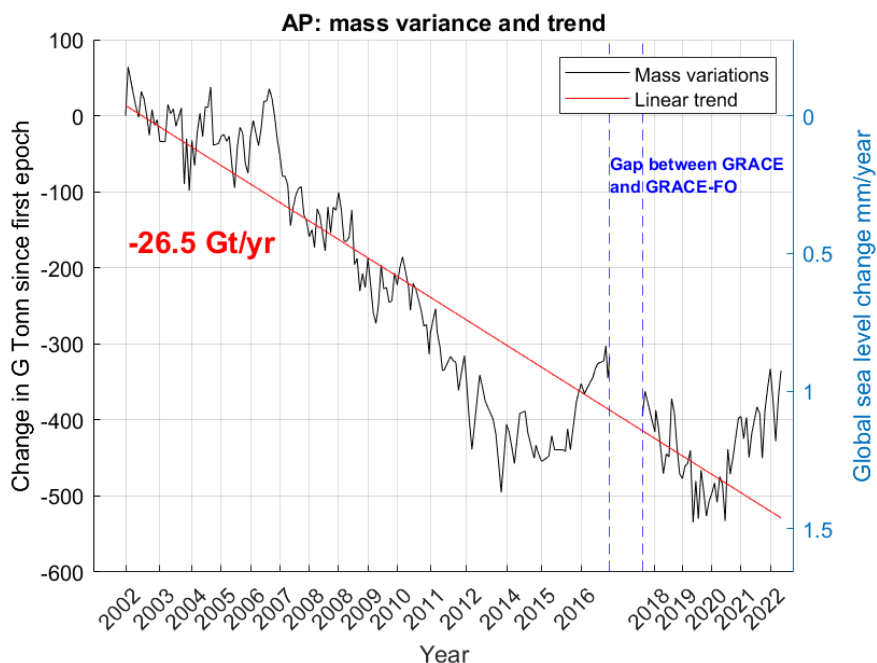
Figure 4.7: Mass variations and trend for AP computed with FM run on each epoch of GSM solution, with cutoff when $|\Delta M|=1\%$ of $|M_{obs}|$, differing mass estimates after FM. Trend computed with the time series 04.2002-11.2022.
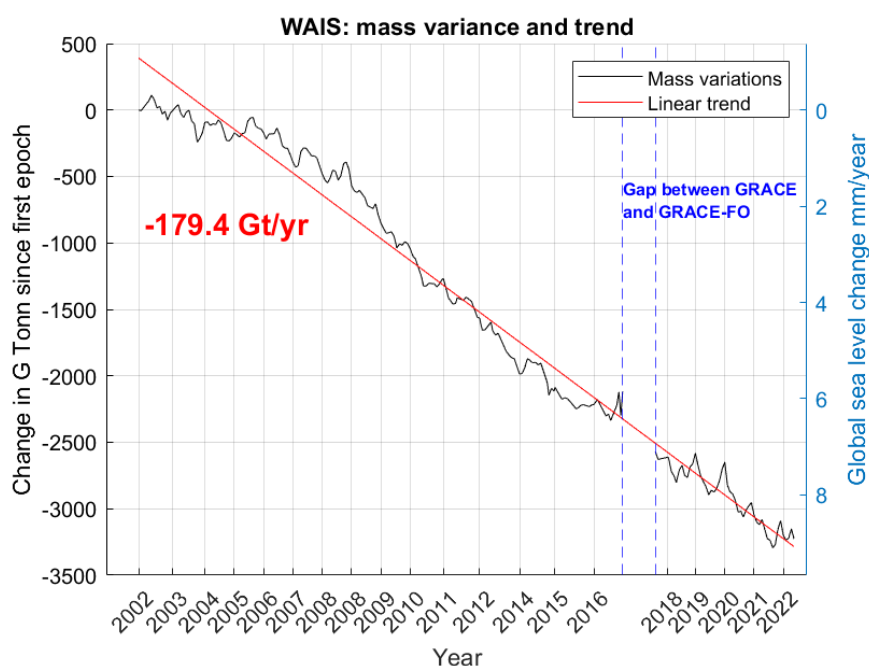
46

Figure 4.8: Mass variations and trend for whole AIS computed with FM run on each epoch of GSM solution, with cutoff when $|\Delta M|=1\%$ of $|M_{obs}|$, differing mass estimates after FM. Trend computed with the time series 04.2002-11.2022.

Figure 4.9: Mass variations and trend for all area in AIS computed with FM run on each epoch of GSM solution, with cutoff when $|\Delta M|=1\%$ of $|M_{obs}|$, differing mass estimates after FM. Trend computed with the time series 04.2002-11.2022.
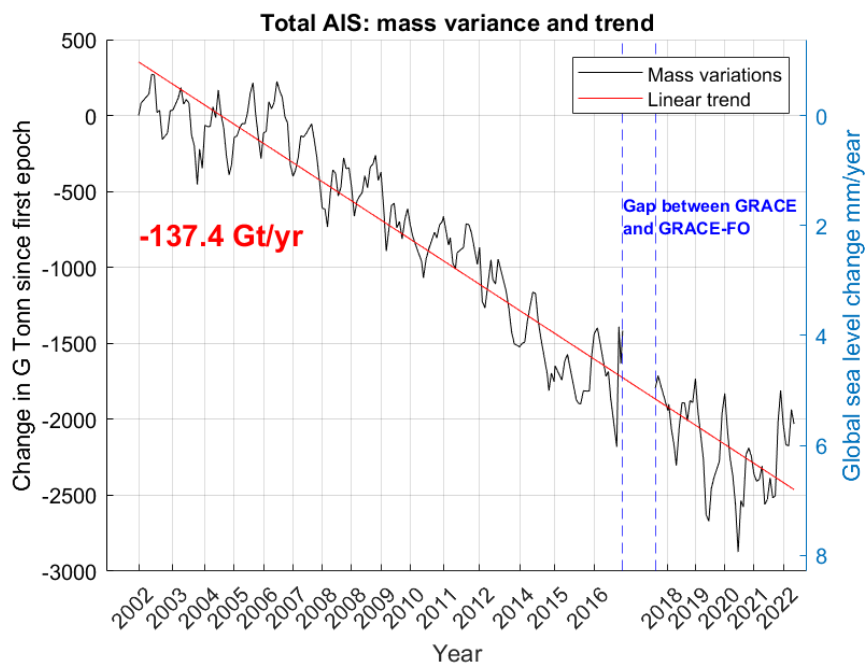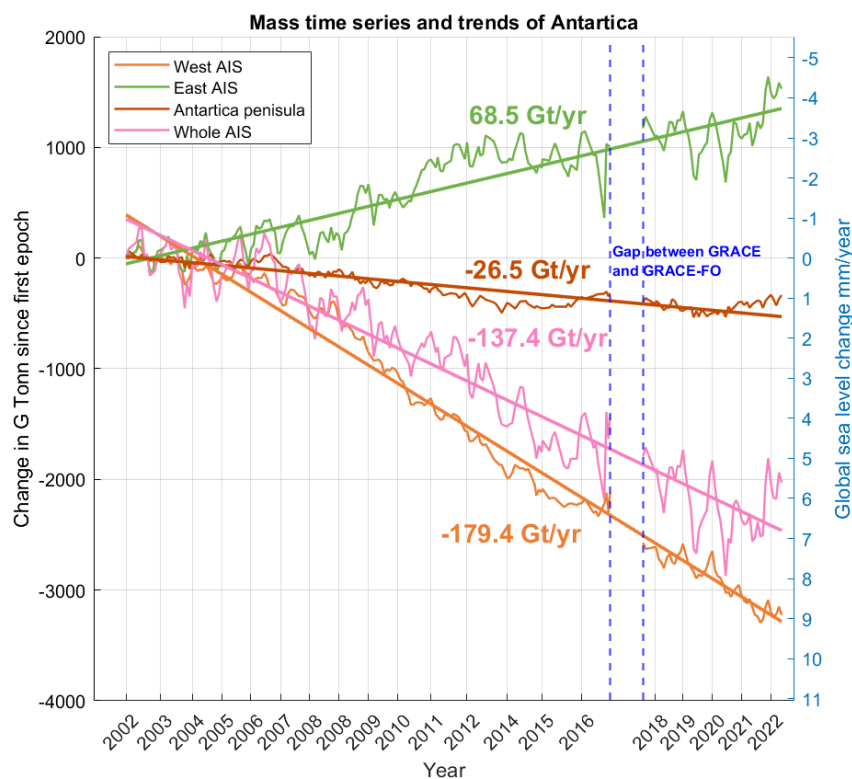
As noticeable the trends in Table 4.7 differ from the trends computed on the coefficients in Table 4.6. The difference between was for WAIS 36, EAIS -8, AP 4, and total AIS 32 Gtonn. The total trends do not significantly differ, however, this is with the GIA model which contains a lot of uncertainty. Without the GIA compensation WAIS, AP and Total AIS trends are significantly different from each other.

It was a bit unexpected that this method didn't produce the same trends as in Table 4.6, from what was shown in section 3.5.2 it was expected to produce the approximate same trends. However, this was before implementing the FM correction. An effort was done to check if the computation technique was wrong.

Since each GSM solution contains a normal field, and in the first attempt with the FM run on each GSM contained these normal fields, the suspicion was raised that 1% of $|M_{obs}|$ would be in the wrong order of magnitude. Another way to compute the trend is to subtract the first epoch of the GSM solution from each following epoch of the GSM solution. This would lead to each solution only containing the difference when the FM was run, and not the entire normal field.

This approach would be differing before the FM, in opposition to the first one where the difference happened after the FM was run. The first results of this approach can be seen in Table 4.8 and Figure 4.10.

Table 4.8: Mass variations and trend for time series from 04.2002-11.2022 for all areas in AIS computed with differing GSM before FM computation with $|\Delta M|$=1% of $|M_{obs}|$. Trends are computed with outliers from FM correction. All units are in Gt/year.

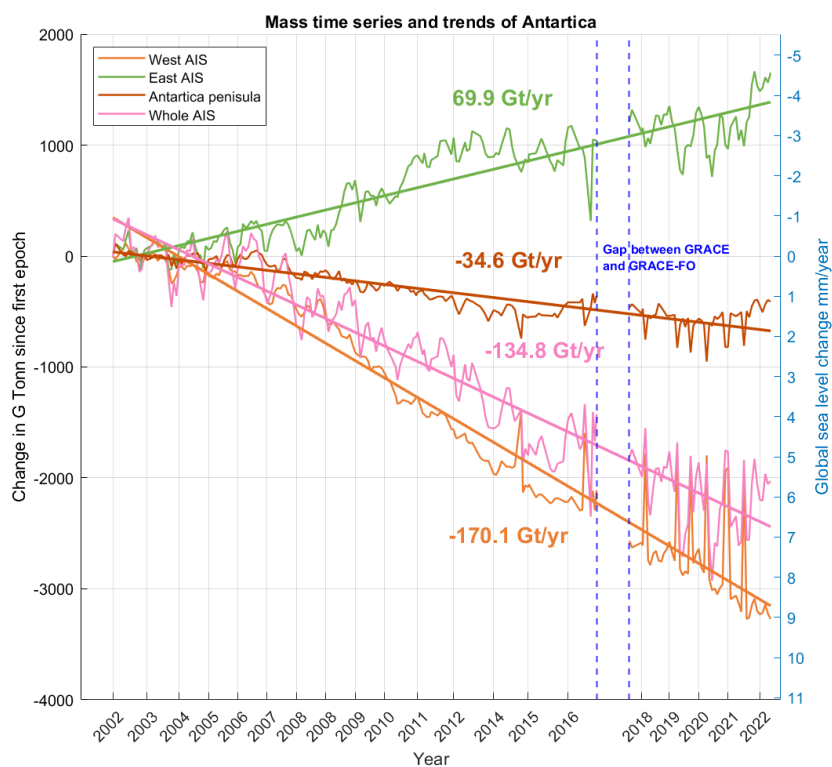| Regions	WAIS	Std	EAIS	Std	AP	Std	Total AIS	Std
Mass estimates with Res = 1°	-126	1	97	2	-31	0	-59	3
ICE6G	44	16	27	15	4	2	76	30
Total	-170	16	70	16	-35	2	-135	31

Figure 4.10: Mass variations and trend for time series from 04.2002-11.2022 for all areas in AIS computed with differing GSM's before FM computation with $|\Delta M|$=1% of $|M_{obs}|$. Contains outliers from FM computation visible in AP, WAIS, and Whole AIS, most frequent in GRACE-FO epochs.

There are clearly noticeable outliers that appear in the WAIS and AP for the most part in the GRACE-FO time series in Figure (4.10). This affects the trend computations. When more thoroughly examined the outliers that are visible correspond to the epochs where the FM used unusually many iterations. One of the GSM epochs used as many as 927 iterations where the mean is at around 10 iterations without these outliers.

So these outliers were removed by checking if a GSM epoch had used more than the standard deviation of the number of iterations a epoch used in the FM computation. Therefore 12 epochs are removed from the trend computation, which should not affect the result much since the epochs removed are from various times, although mostly in the GRACE-FO period. The result of removing these outliers can be seen in Table 4.9, Figure 4.11, 4.12, 4.13, 4.14, and 4.15.

The method of differentiating the GSM solutions before running the FM do not make a significant difference when the differentiating happens after the FM, except AP which is significantly different. The difference in trend between Table 4.7 and Table 4.9 are, WAIS -0.1 Gt/year, EAIS 4,2 Gt/year, AP -5, and total AIS -1,8 Gt/year. It is important to bear in mind that in Table 4.9 12 epochs of GSM have been removed, and can probably be a reason why the trends presented in Table 4.7 and Table 4.9 are different.

Table 4.9: Mass variations and trend for time series from 04.2002-11.2022 for all areas in AIS computed with differing GSM before FM computation with $|\Delta M|$=1% of $|M_{obs}|$. The Outliers from FM iteration are removed when the trends are computed. All units are in Gt/year.

Regions	WAIS	Std	EAIS	Std	AP	Std	Total AIS	Std
Mass estimates with Res = 1°	-135	1	100	2	-28	0	-63	3
ICE6G	44	16	27	15	4	2	76	30
Total	-180	16	73	16	-32	2	-139	31

Figure 4.11: Mass variations and trend for WAIS with the time series from 04.2002-11.2022 for all areas in AIS computed with differing GSM before FM computation with $|\Delta M|$=1% of $|M_{obs}|$. Outliers from FM iteration are removed . All units are in Gt/year.
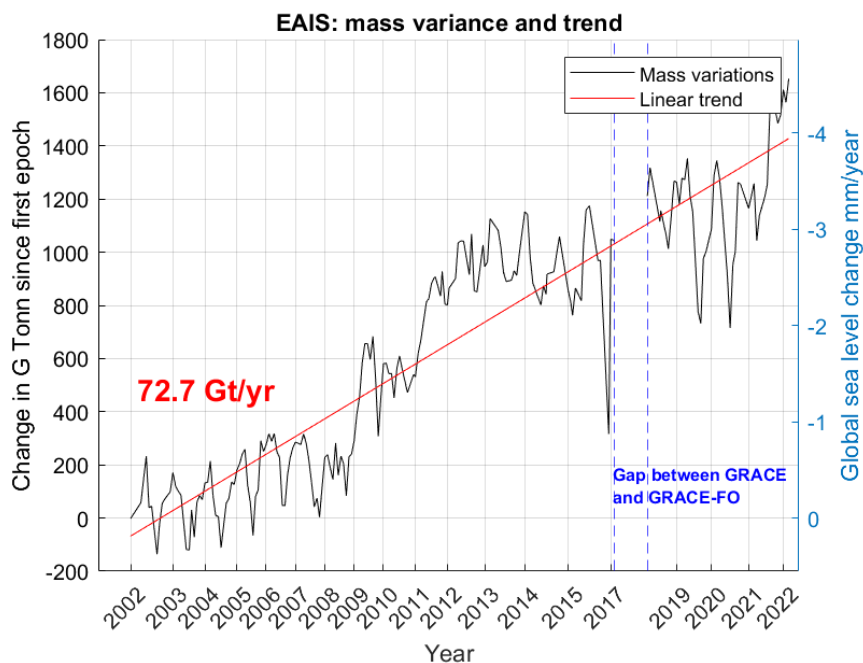
Figure 4.12: Mass variations and trend for EAIS with the time series from 04.2002-11.2022 for all areas in AIS computed with differing GSM before FM computation with $|\Delta M|$=1% of $|M_{obs}|$. Outliers from FM iterations removed . All units are in Gt/year.
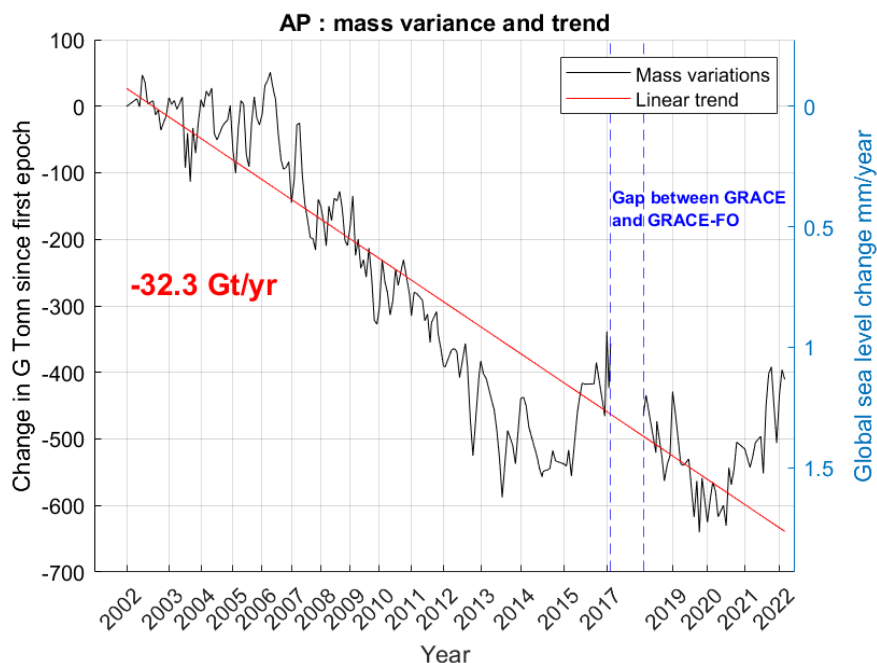
Figure 4.13: Mass variations and trend for AP with the time series from 04.2002-11.2022 for all areas in AIS computed with differing GSM before FM computation with $|\Delta M|$=1% of $|M_{obs}|$. Outliers from FM iterations removed . All units are in Gt/year.

Figure 4.14: Mass variations and trend for whole AISwith the time series from 04.2002-11.2022 for all areas in AIS computed with differing GSM before FM computation with $|\Delta M|$=1% of $|M_{obs}|$. Outliers from FM iterations removed . All units are in Gt/year.
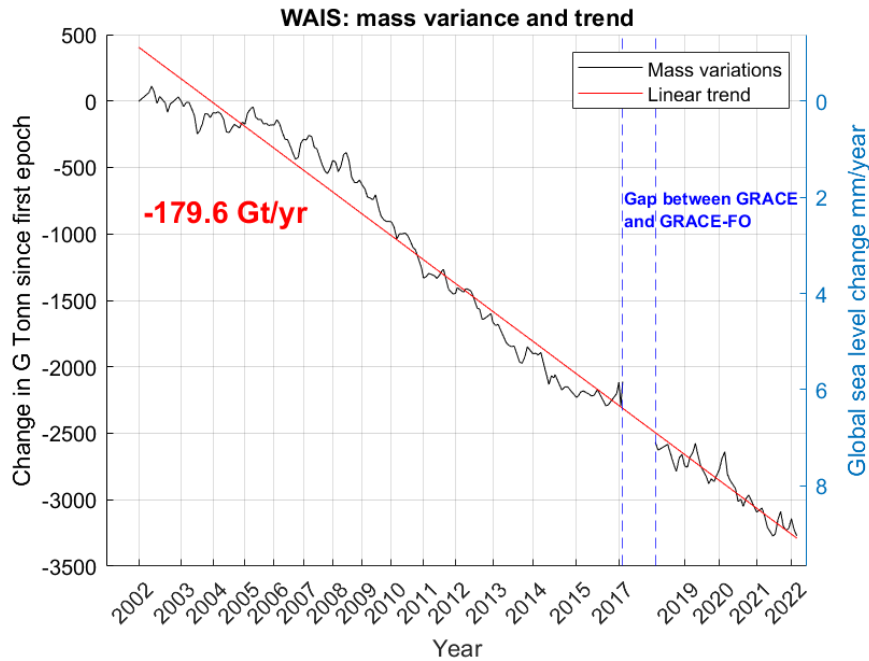

Figure 4.15: Mass variations and trend for all areas in AIS with the time series from 04.2002-11.2022 for all areas in AIS computed with differing GSM before FM computation with $|\Delta M|$=1% of $|M_{obs}|$. Outliers from FM iterations removed . All units are in Gt/year.
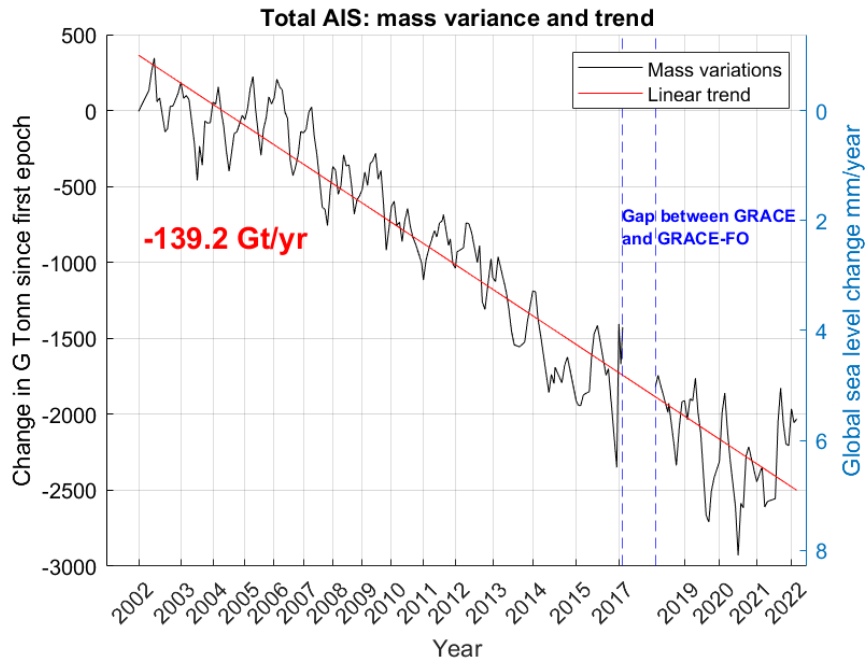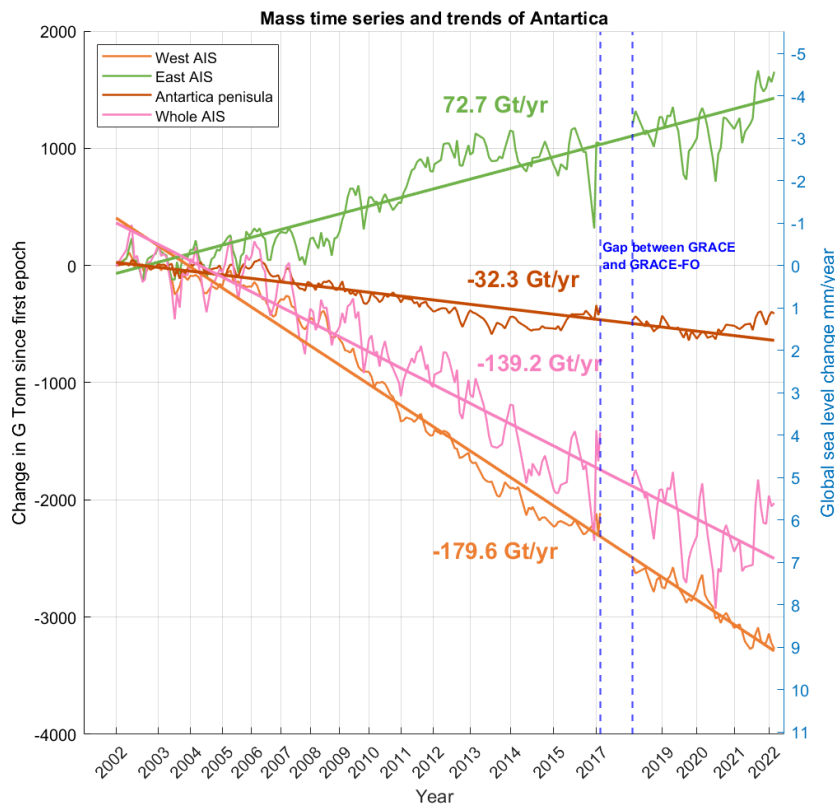
The trend for the mass estimates without the GIA correction computed by running the FM on each GSM epoch is significantly different from FM computed on the trend from the coefficients. However, it is possible to use the figures in this section to look at the variations. From Figure 4.9 and Figure 4.15 it is clearly visible that there are season variations affecting the ice masses in AIS. The trend in EAIS is a bit surprising suggesting that the continent accumulates ice mass. This can be explained by bigger precipitation events happening as a course of large weather patterns like El Nino, and wind patterns in EAIS driving snow masses towards the pole (Boening et al., 2012). The trends in AP and WAIS are in decline and it seems like it is not as affected by seasonal variations as EAIS. However in Figure 4.9 and Figure 4.15, the scale of the area for EAIS will perhaps make the amplitude of season variations higher.

In WAIS the great mass loss can be explained by marine-terminating glaciers in the Amundsen Sea Embayment. Located here are Pine Island, Thwaites, Haynes, Pope, Smith and Kohler Glaciers and is well documented to have a large mass loss (Loomis et al., 2021). Even though the AP don not have large glaciers as WAIS has, it is vulnerable to change through its small size and its relative northern latitude which is more affected of ocean tempratures (Davies et al., 2012).

4.2.3 Mascon solutions for the time span 04.2002-11.2022

It is possible to compare the previous trends in this section with the mascons from JPL and GSFC for the same time span, this can be seen in Table 4.10 and Figure 4.16 and 4.17.

The trends presented here are not significantly different from the trends presented in Table 4.6 for WAIS, EAIS, and Total AIS, AP is again significantly different. This suggests that the trend was calculated on the coefficients and then run an FM on are probably more correct than the FM run on each epoch. This also makes sense with the proof of concept, where the FM on each epoch where proven to not significantly differ from the results in Loomis et al. (2021).

Table 4.10: The trend calculated from GSFC and JPL mascons with standard deviation for 04.2002-11.2022. All units in Gtonn/year.

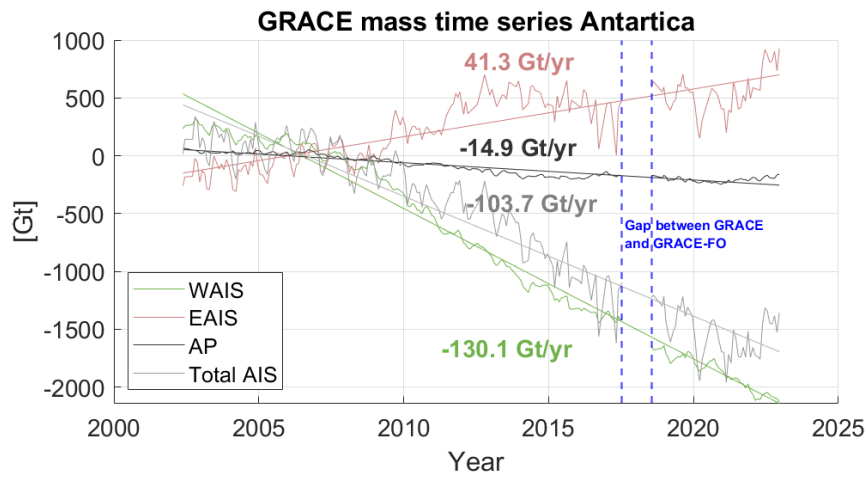| Regions	WAIS	Std	EAIS	Std	AP	Std	Total AIS	Std
GSFC corrected for GIA	-130	1	41	2	-15	0	-104	2
JPL corrected for GIA	-144	1	49	2	-14	0	-109	2

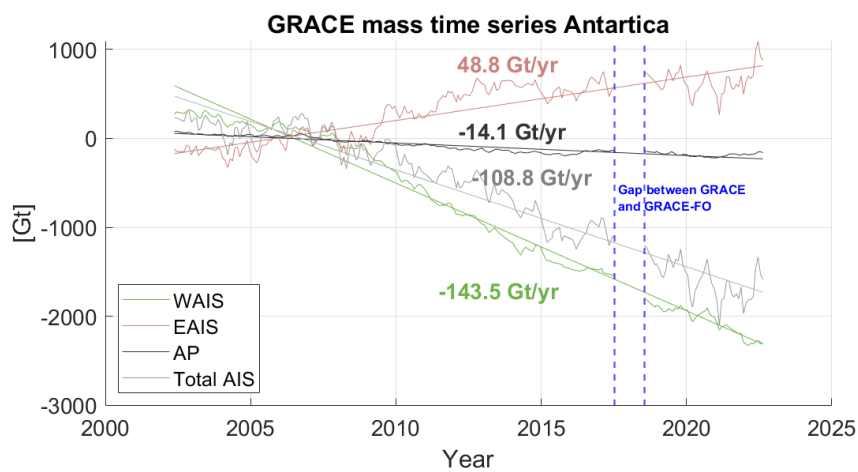Figure 4.16: The mass trend and variations derived from the GSFC mascon for 04.2002-11.2022.

Figure 4.17: The mass trend and variations derived from the JPL mascon for 04.2002-11.2022.

4.2.4 The trend with different time span

One solution to consider if the mass trends in AIS are accelerating or decelerating is to divide the whole GRACE and GRACE-FO gravity mission up in parts and look at trends for different time spans. This is done with 6 time spans and calculated a trend on the coefficients with the FM to correct for leakage, and can be seen in Table 4.11.

It is divided to look at the trend for 36 epochs each, not considering the missing epochs between GRACE and GRACE-FO, and other missing months. This gives a trend period each of around 3 years. The division into 36 epochs for each time span was out of practicality to get even time spans from the 215 epochs available.

There are a lot of interesting aspects in Table 4.11. The uncertainties are higher because there are fewer epochs to compute each trend. WAIS and EAIS vary throughout the different time span. Especially EAIS from positive to negative trends. From the trends presented earlier in this chapter, EAIS would not be expected to have a negative trend. WAIS has a negative for all the time spans, the same applies for AP except for the last epoch 01.2020-11.2022. This seems to be the same for the total AIS mass trends. It accelerates until the last timespan where EAIS and AP have mass gain enough to make the total AIS gain 125 Gt/year.

The method of dividing into smaller time spans can give some insight into how the trend is developing, however, the long-term trend is not that well represented with this method. The last epoch would indicate that the trend is decelerating, however, without the last epoch it seems like the trend is accelerating. With the variations that especially WAIS has it is hard to say if the trend is decelerating.

Table 4.11: An table showing the trend for 6 time spans: 04.2002-06.2005, 07.2005-06.2008, 07.2008-08.2011, 09.2011-04.2015, 05.2015-12.2019, and 01.2020-11.2022. The trends are computed on the coefficients with the FM to compensate for leakage. The GIA effect from the ICE6G-C model is the same for all time spans and is therefore left out, the GIA corrections are: WAIS 44 ±16, EAIS 27 ±15, AP 4 ±2, and total AIS 76 ±30. All units are in Gt/year.

Epoch	1-36		36-72		72-108		109-144		144-180		180-215	
time span	04.02 - 06.05		07.05 - 06.08		07.08 - 08.11		09.11 - 04.15		05.15 - 12.19		01.20 - 11.22	
	Mass	Std	Mass	Std	Mass	Std	Mass	Std	Mass	Std	Mass	Std
GRACE derived mass trend estimates												
WAIS	-28	16	-67	16	-203	17	-140	13	-112	11	-95	18
EAIS	46	32	24	32	151	33	27	26	-20	22	241	36
AP	-11	5	-34	5	-32	5	-35	4	-13	3	54	6
Total AIS	7	36	-77	36	-84	37	-148	29	-144	25	200	40
Total corrected for GIA with ICE6G-C												
WAIS	-72	22	-111	23	-247	23	-185	21	-156	19	-139	24
EAIS	19	35	-3	36	124	36	0	20	-47	27	213	39
AP	-15	5	-38	5	-36	5	-39	26	-17	4	50	6
Total AIS	**-69**	47	**-153**	47	**-160**	48	**-224**	31	**-220**	39	**125**	50

Chapter 5

Discussion

5.1 Proof of concept

The total trends shown in Table 4.1 from Loomis et al. (2021) are not significantly different from the total trends computed in this thesis shown in Table 4.2, 4.3 and 4.4.

When it comes to the parts of the total trend, GIA and GRACE derived mass trend estimates the results of this thesis differ from the results in Loomis et al. (2021). None of the GIA estimates computed in this thesis are significantly different from the ones given in Loomis et al. (2021), however, they differ up to 21 Gt/year for the total AIS area. The GIA model contains much uncertainty and therefore rarely significantly different. Fortunately the same is the case with the GRACE-derived mass estimates as well. None of them are significantly different from the results in Loomis et al. (2021), however, they tend to differ in the same order of magnitude as the GIA differences. The contributions from GRACE-derived mass and GIA will in both cases for the computations in this thesis and in the results from Loomis et al. (2021) add up to the same total effect.

The uncertainties computed in this thesis in Table 4.2, 4.3 and 4.4 and from Loomis et al. (2021) in Table 4.1 differ. In the uncertainties seen in Table 4.2, 4.3 and 4.4 the main part of the total signal uncertainty originates from the uncertainties from the GIA data. The computations of the uncertainties for the ICE6G-GIA data are different in Loomis et al. (2021) and in this thesis, however, the uncertainties are in the same order of magnitude. There are many ways of deciding the uncertainties in GIA models and the results vary. When dealing with global GIA models the uncertainties are usually high, especially in AIS areas where the data foundation is not as large as other areas.

The standard deviation for the GRACE part of mass estimates trends in Loomis et al. (2021) seen in Table 4.1 is computed from the total (GIA corrected) and GIA standard deviation given in Table 2 in Loomis et al. (2021). This differs from the standard deviations computed in this thesis, by an order of magnitude. The reason as mentioned before is that Loomis et al. (2021) uses a combination with the GOCO-06S spherical harmonic products, and creates empirical uncertainty by comparing it to other models. The uncertainties computed in this thesis, however, are derived through formal error propagation of the standard deviation given to each spherical harmonic coefficient and are therefore formal errors. Thus the uncertainties are not directly comparable and the uncertainties computed in this thesis will be a bit optimistic. The approach of Loomis et al. (2021) to compute the uncertainties could be possible for further work.

There are trends derived from the mascon delivered by GFSC and JPL in the same areas and time series, as computations in this thesis and in Loomis et al. (2021). The trends derived from the mascons as mentioned in section 4.1.3 do not significantly differ from the trends computed and in Loomis et al. (2021), however, they differ. The total AIS trend seems to be around 20 Gt/year lower for the mascon trends than the trends in Loomis et al. (2021) and in this thesis. The reason they do not significantly differ would be the large uncertainty deriving from the GIA models as discussed above.

The uncertainties connected to the mascon trends are also a bit optimistic. The mascon contains already ICE6G GIA corrections so it would be expected that the uncertainties would be significantly higher.

To summarize the total trends computed in this thesis are comparable with the trends of Loomis et al. (2021), which gives confidence in the correctness of the computations in this thesis.

5.2 Inclusion of GRACE-FO data

By looking at the inclusion of GRACE-FO data it would be interesting to see if the mass change trends in AIS are accelerating, stable, or decelerating.

When the trend calculated from coefficients from the time period 04.2002-11.2022 in Table 4.6 is compared with the time period of Loomis et al. (2021) 04.2002-08.2016 in Table 4.3, all the total trends are not significantly different. The same applies to the GRACE estimates in WAIS, EAIS, and total AIS, however, the trends for AP differ significantly. The difference for AP is 9,7 Gt/year, resulting in a deceleration from -28,2 Gt/year to -18,5 Gt/year. For WAIS the difference is 3,7 Gt/year, EAIS -2,4 Gt/year, and total AIS 10,9 Gt/year where the biggest part derives from AP.

The area of AP is smaller than WAIS and EAIS, which can make it more vulnerable when detecting using GRACE. The small area combined with GRACE relatively large spatial resolution can contribute to misclassifying the gravity signals emerging from AP. In Figure 4.2 the AP area is shown, the possibility of misclassifying, bear in mind that Figure 4.2 shows the trend with a spatial resolution of 0,5°.

5.2.1 The difference in FM on trend computed on coefficients and FM on each epoch

It was a bit astonishing to get different results when the FM was run on each epoch of GSM. In section 3.5.2 it was established that the difference when the trend is calculated with three different methods would not create a significant difference. However, this was before implementing the FM to the trend computations. The FM must therefore be properly examined to hopefully understand why this creates the differences in trend estimation.

These are some points that should be examined further in future work to solve this problem.

- The border areas of AIS should be investigated more, especially the coastal pixels that are of interest. In WAIS the trend is largest along the coast, most likely given that this is where the ice sheets calves. The outliers seen in Figure 4.10 could perhaps be explained by some coastal pixel that could be misinterpreted. The outliers are also visible in the same epochs for WAIS and AP and it could also be explained by a misinterpretation of the pixels along the border between the areas.

- Redistributing the mass to the global ocean for each iteration as mentioned in section 3.6.1 is left out of the FM made in this thesis. This can have implications on the estimates in a larger part when the FM is computed on each epoch and not the trend.

- The outliers created by the wrongfully run FM on 12 of the epochs, should be looked more into. When the $|\Delta M|$ of each iteration is looked at, the first iteration gets an extreme value. This leads to the FM iterating many times before $|\Delta M|=1\%$ of $|M_{obs}|$. So far an explanation of the extreme first iteration is not discovered and would need further investigation. The outliers and the extreme values itself does not explain the different trends, however the bugs creating the outliers can be connected to why the trends differ.

The reason for running the FM on each epoch was to create reasonable mass variations and trend graphs seen in section 4.2.2. The assumption was that it was necessary to apply an FM to each epoch to create mass estimates and a graph representing the mass variations correctly. Without this the amplitude of the mass variations in AIS would have been significantly lower and comparable to the ones presented in Table 3.1.

The mass trends from the JPL and GSFC shown in Table 4.10 are much closer to the trends calculated with the coefficients. This further scrutinizes the results presented in section 4.2.2, FM on each epoch of GSM.

To bring more clarity to which of the trend computation methods gives the most correct trends some other studies can be looked at. In Velicogna et al. (2020) there is a time series from 04.2002-09.2019 where the total mass trend for AIS is -107±55 Gt/yr for CSR, -104±57 Gt/yr for JPL, and -89±60 Gt/yr for GFZ. All these total trends are significant like the ones computed with FM on the trend from the coefficients and FM on each GSM epoch. However, the trend from FM on the trend from the coefficients differs -2,1 Gt/year with the CSR solution, 0.9 Gt/year with the JPL solution, and 15,9 Gt/year with GFZ solution.
With the method FM on each GSM epoch, they differ 30,4 Gt/year for CSR, 33,4 for JPL, and 48,4 for GFZ. From these differences, it seems like the method of FM on the trend from the coefficients is the correct way to calculate the trend. However, it is important to bear in mind that Velicogna et al. (2020) does not use the same time period as did in this thesis.

It is more likely that the method with FM on the trend calculated on the coefficients is the right approach, since the results are in the same scale for Velicogna et al. (2020) and in the mascons from JPL and GSFC.

5.2.2 Acceleration or decelerating mass trends

There are presented two ways to tell if the trends are accelerating or decelerating in this thesis. Comparing the trends from long-time series as the time period Loomis et al. (2021) used with GFO included time period or comparing relative short time spans with each other as presented in Table 4.11.

From comparing the time series 04.2002-08.2016 with 04.2002-11.2022 the trend would seem to decelerate. This also seems to be the when comparing relatively short time spans as in section 4.2.4, however, it also establishes that the trend is not that stable and can change relatively fast. The EAIS would appear to be the most driving part of the variations in trend. As suggested in Boening et al. (2012) the accumulating can coincide with weather systems causing snowfall and winds to add or redistribute masses. If this effect is large enough it could explain the large variations in EAIS.

What could have been considered when making this division of the time series, was to divide

them into time spans corresponding to weather phenomena. The time spans in Table 4.11 could line up badly with weather phenomena. A starting period of a driving force for precipitation or winds could happen at the end of the time span in Table 4.11, and it could end in the middle of a time span. Further criticism could be that Table 4.11 should have lined up with the time spans in Table 2. in Martín-Español et al. (2016). This would have made for a rather interesting comparison.

5.2.3   Further criticism of solutions in this thesis

There are parts that have not been included in this thesis which are possible and are done in the literature followed. This is to summarize and might give some clue to the differences seen.

- **Inclusion of seismic activity** . As described in section 4.1.1 and in Loomis et al. (2021) removes three earthquakes. This is not done in the computations of this thesis and could affect the results in some way. The earthquakes are not in AIS but they affect the global mass distribution.

- **Restoring ocean mass**. As described in Chen et al. (2015) to conserve total water mass a uniform layer of water is added or subtracted from the oceans. This is not done in this thesis and can contribute to some errors while running the FM.

Chapter 6

Concluding remarks

6.1 Trend

The ambition of this thesis was to find trends for the cryosphere in Antarctica. There are presented several trends in this thesis, however, the trend of most interest is the latest one, computed with the time period from 04.2002 til 11.2022. For the whole AIS area, this trend is -105 ± 31 Gt/year. The trend seems to decelerate when compared to the time period from 04.2002 til 11.2016.

The total trend consists of WAIS, EAIS and AP, both the trend and its deceleration in the whole area need to be looked at with these areas in mind.

The EAIS area has perhaps surprisingly a positive trend accumulating masses. One explanation for this can be extensive snowfall in periods and polewards wind patterns moving snow masses (Boening et al., 2012). The large negative trends in WAIS can be explained by the large marine-terminating glaciers located there. The negative trend in AP likely occurs since it has a relatively small size and a relatively northern location and is therefore vulnerable to shifting ocean temperatures. The trend from WAIS, EAIS, and AP in the time period from 04.2002-11.2022 is compared with the trend in the time period from 04.2002 til 08.2016, gives that WAIS is decelerating its mass loss by 3,7 Gt/year, EAIS's rising trend is decelerating with a mass loss with -2,4 Gt/year and AP decelerating its mass loss with 9,7 Gt/year. When the time period from 04.2002-11.2022 is divided into 6 parts it appears that the total trend accelerates in 5 first parts but in the last part, it decelerates significantly compared to the fifth.

6.2 Comparisons to understand the size of the trends

The terms in Gtonn and global sea-level change are sizes that are not easy to relate to so this section will try to set up some scale of how large the mass changes in AIS actually are. This section will look at only the total AIS change corrected for GIA, which yearly is -105 Gt, and this would have accumulated to a mass change of -2098 Gt for the 20 years since the launch of GRACE, from 04.2002 to 11.2022.

6.2.1 Sea-level change

The sea-level change was proposed in the figures in section 4.2.2 as a more understandable means to understand the mass changes. Unfortunately as explained in section 5.2 the results are not entirely dependable. With the assumption 1mm Global mean sea-level = 362Gtonn

as in section 5.2 we get that contribution from AIS to the global mean sea-level makes it rise yearly with 0,3mm and a total accumulated rise from 04.2002 to 11.2022 at 5,8mm.

6.2.2   Ice cover in Norway

The area of mainland Norway is estimated to be 323 810 km^2 (Kartverket, 2022). If the mass trend in the AIS were evenly distributed as a layer of ice across the entire mainland of Norway, it would grow at a rate of 27 cm per year. If the ice that had accumulated mass loss from the AIS between April 2002 and November 2022 was spread out over Norway's mainland, it would create a uniform layer of ice 5,5 meters thick.

6.2.3   Volumes

If the mass changes were deconstructed into massive ice cubes there would be a yearly ice cube with sides of 4,7km each. And the accumulated mass loss would create an ice cube with sides of 12,8 km.

To compare the volume of the mass change each year would dry out Mjøsa Norway's largest lake almost 2 times a year. The volume of Mjøsa is 56 km^3 (Petterson, 1997) and the yearly mass change volume is -105 km^3.

To put it in a commonly used volume parameter, however not so suitable, the yearly trend will fill up about 84 million Olympic swimming pools.

6.3   Recommendations for further work

For any further work, some recommendations will be given.

Area borders both between AIS areas and against the ocean could be investigated further. The chance of integrating an area twice should be left out and the highest mass trends occur in the coastal areas which underscore the significance of accurate classification in this region.

The FM can be improved by redistributing the mass change as a uniform layer of water over the global oceans. Further the FM should be investigated and determine why it can use as many iterations as it does with some of the epochs. This should give some insight into why the trend differs between the two computation methods.

When dividing larger time series into smaller time spans, the occurrence of large weather patterns should be kept in mind. With time spans that follow large weather patterns, connections to the trends could be made.

Lastly, the inclusion of different models from the SDS or COST-G would have led to more comparisons and possibly a more accurate determination of the variation and trend.

Bibliography

Boening, C., Lebsock, M., Landerer, F. and Stephens, G. (2012), 'Snowfall-driven mass change on the East Antarctic ice sheet', *Geophysical Research Letters* **39**(21).

Caron, L., Ivins, E. R., Larour, E., Adhikari, S., Nilsson, J. and Blewitt, G. (2018), 'GIA Model Statistics for GRACE Hydrology, Cryosphere, and Ocean Science', *Geophysical Research Letters* **45**(5), 2203–2212.

Chen, J., Cazenave, A., Dahle, C., Llovel, W., Panet, I., Pfeffer, J. and Moreira, L. (2022), 'Applications and Challenges of GRACE and GRACE Follow-On Satellite Gravimetry'.

Chen, J. L., Wilson, C. R., Li, J. and Zhang, Z. (2015), 'Reducing leakage error in GRACE-observed long-term ice mass change: a case study in West Antarctica', *Journal of Geodesy* **89**(9), 925–940.

Cheng, M., Ries, J. C. and Tapley, B. D. (2011), 'Variations of the Earth's figure axis from satellite laser ranging and GRACE', *Journal of Geophysical Research* **116**(B1), B01409.

Davies, B. J., Hambrey, M. J., Smellie, J. L., Carrivick, J. L. and Glasser, N. F. (2012), 'Antarctic Peninsula Ice Sheet evolution during the Cenozoic Era', *Quaternary Science Reviews* **31**, 30–66.

Dorschel, B., Hehemann, L., Viquerat, S., Warnke, F., Dreutter, S., Tenberge, Y. S., Accettella, D., An, L., Barrios, F., Bazhenova, E., Black, J., Bohoyo, F., Davey, C., De Santis, L., Dotti, C. E., Fremand, A. C., Fretwell, P. T., Gales, J. A., Gao, J., Gasperini, L., Greenbaum, J. S., Jencks, J. H., Hogan, K., Hong, J. K., Jakobsson, M., Jensen, L., Kool, J., Larin, S., Larter, R. D., Leitchenkov, G., Loubrieu, B., Mackay, K., Mayer, L., Millan, R., Morlighem, M., Navidad, F., Nitsche, F. O., Nogi, Y., Pertuisot, C., Post, A. L., Pritchard, H. D., Purser, A., Rebesco, M., Rignot, E., Roberts, J. L., Rovere, M., Ryzhov, I., Sauli, C., Schmitt, T., Silvano, A., Smith, J., Snaith, H., Tate, A. J., Tinto, K., Vandenbossche, P., Weatherall, P., Wintersteller, P., Yang, C., Zhang, T. and Arndt, J. E. (2022), 'The International Bathymetric Chart of the Southern Ocean Version 2', *Scientific Data* **9**(1), 275.

Gerlach, C. and Fecher, T. (2012), 'Approximations of the GOCE error variance-covariance matrix for least-squares estimation of height datum offsets', *Journal of Geodetic Science* **2**(4), 247–256.

Hofmann-Wellenhof, B. and Moritz, H. (2006), *Physical Geodesy*, 2 edn, Springer, Wien.

Jekeli, C. (1981), Alternative methods to smooth the Earth's gravity field, Technical report, Department of Geodetic Science and Surveying, The Ohio State University, Ohio.

Kartverket (2022), 'Kor stort er Noreg?'.
URL: *https://www.kartverket.no/til-lands/fakta-om-norge/storleiken-pa-landet*

Kusche, J. (2007), 'Approximate decorrelation and non-isotropic smoothing of time-variable GRACE-type gravity field models', *Journal of Geodesy* **81**(11), 733–749.

Kusche, J., Schmidt, R., Petrovic, S. and Rietbroek, R. (2009), 'Decorrelated GRACE time-variable gravity solutions by GFZ, and their validation using a hydrological model', *Journal of Geodesy* **83**(10), 903–913.

Kvas, A., Brockmann, J. M., Krauss, S., Schubert, T., Gruber, T., Meyer, U., Mayer-Gürr, T., Schuh, W.-D., Jäggi, A. and Pail, R. (2021), 'GOCO06s – a satellite-only global gravity field model', *Earth System Science Data* **13**(1), 99–118.

Loomis, B. D., Felikson, D., Sabaka, T. J. and Medley, B. (2021), 'High-Spatial-Resolution Mass Rates From GRACE and GRACE-FO: Global and Ice Sheet Analyses', *Journal of Geophysical Research: Solid Earth* **126**(12).

Loomis, B. D., Rachlin, K. E. and Luthcke, S. B. (2019), 'Improved Earth Oblateness Rate Reveals Increased Ice Sheet Losses and Mass-Driven Sea Level Rise', *Geophysical Research Letters* **46**(12), 6910–6917.

Loomis, B. D., Rachlin, K. E., Wiese, D. N., Landerer, F. W. and Luthcke, S. B. (2020), 'Replacing GRACE/GRACE-FO With Satellite Laser Ranging: Impacts on Antarctic Ice Sheet Mass Change', *Geophysical Research Letters* **47**(3).

Martín-Español, A., Zammit-Mangion, A., Clarke, P. J., Flament, T., Helm, V., King, M. A., Luthcke, S. B., Petrie, E., Rémy, F., Schön, N., Wouters, B. and Bamber, J. L. (2016), 'Spatial and temporal Antarctic Ice Sheet mass trends, glacio-isostatic adjustment, and surface processes from a joint inversion of satellite altimeter, gravity, and GPS data', *Journal of Geophysical Research: Earth Surface* **121**(2), 182–200.

Peltier, W. R., Argus, D. F. and Drummond, R. (2015), 'Space geodesy constrains ice age terminal deglaciation: The global ICE-6G-C (VM5a) model', *Journal of Geophysical Research: Solid Earth* **120**(1), 450–487.

Petterson, L.-E. (1997), Hydrologiske data for Mjøsa, Technical report, NVE Norges Vassdrag og Energiverk, Oslo.

Rignot, E., Mouginot, J. and Scheuchl, B. (2011), 'Antarctic grounding line mapping from differential satellite radar interferometry', *Geophysical Research Letters* **38**(10).

Seeber, G. (2003), *Satellite Geodesy*, 2 edn, Walter de Gruyter, Berlin.

Sun, Y., Riva, R. and Ditmar, P. (2016), 'Optimizing estimates of annual variations and trends in geocenter motion and J2 from a combination of GRACE data and geophysical models', *Journal of Geophysical Research: Solid Earth* **121**(11), 8352–8370.

Sun, Y. and Riva, R. E. (2020), 'A global semi-empirical glacial isostatic adjustment (GIA) model based on Gravity Recovery and Climate Experiment (GRACE) data', *Earth System Dynamics* **11**(1), 129–137.

Swenson, S., Chambers, D. and Wahr, J. (2008), 'Estimating geocenter variations from a combination of GRACE and ocean model output', *Journal of Geophysical Research: Solid Earth* **113**(B8).

Tapley, B. D., Watkins, M. M., Flechtner, F., Reigber, C., Bettadpur, S., Rodell, M., Sasgen, I., Famiglietti, J. S., Landerer, F. W., Chambers, D. P., Reager, J. T., Gardner, A. S., Save, H., Ivins, E. R., Swenson, S. C., Boening, C., Dahle, C., Wiese, D. N., Dobslaw, H., Tamisiea, M. E. and Velicogna, I. (2019), 'Contributions of GRACE to understanding climate change'.

Torge, W. and Müller, J. (2012), *Geodesy*, 4 edn, Walter de Gruyter GmbH & Co., Berlin/Boston.

Velicogna, I., Mohajerani, Y., Geruo, A., Landerer, F., Mouginot, J., Noel, B., Rignot, E., Sutterley, T., van den Broeke, M., van Wessem, M. and Wiese, D. (2020), 'Continuity of Ice Sheet Mass Loss in Greenland and Antarctica From the GRACE and GRACE Follow-On Missions', *Geophysical Research Letters* **47**(8).

Wahr, J. and Molenaar, M. (1998), 'Time variability of the Earth's gravity field: Hydrological and oceanic effects and their possible detection using GRACE', *Journal of Geophysical Research: Solid Earth* **103**(B12), 30205–30229.

Watkins, M. M., Wiese, D. N., Yuan, D.-N., Boening, C. and Landerer, F. W. (2015), 'Improved methods for observing Earth's time variable mass distribution with GRACE using spherical cap mascons', *Journal of Geophysical Research: Solid Earth* **120**(4), 2648–2671.

Wen, H. W., Kruizinga, G., Paik, M., Landerer, F., Bertiger, W., Sakumura, C., Bandikova, T. and Mccullough, C. (2019), Gravity Recovery and Climate Experiment Follow-On (GRACE-FO) Level-1 Data Product User Handbook, Technical report, JPL, California.

Whitehouse, P. L. (2018), 'Glacial isostatic adjustment modelling: Historical perspectives, recent advances, and future directions', *Earth Surface Dynamics* **6**(2), 401–429.

Wiese, D., Yuan, D.-N., Boening, C., Landerer, F. and Watkins, M. M. (2023), JPL GRACE and GRACE-FO Mascon Ocean, Ice, and Hydrology Equivalent Water Height Coastal Resolution Improvement (CRI) Filtered Release 06.1 Version 03, Technical report, CA, USA.